



## An h-adaptive thermo-mechanical phase field model for fracture



Hojjat Badnava<sup>a,\*<sup>1</sup></sup>, Mohammed A. Msekh<sup>b,\*\*<sup>1</sup></sup>, Elahe Etemadi<sup>c</sup>, Timon Rabczuk<sup>d</sup>

<sup>a</sup> Department of Mechanical Engineering, Behbahan Khatam Alania University of Technology, Khuzestan, Iran

<sup>b</sup> Civil Engineering Department, College of Engineering, University of Babylon, Babylon, Iraq

<sup>c</sup> Faculty of Engineering, Semnan University, Semnan, Iran

<sup>d</sup> Institute of Structural Mechanics, Faculty of Civil Engineering, Bauhaus-University Weimar, Germany

### ARTICLE INFO

#### Keywords:

Phase field model  
Thermal induced cracks  
Brittle fracture  
Thermo-mechanical fracture  
Mesh refinement

### ABSTRACT

In this work, brittle fracture and thermo-mechanical induced cracks are simulated using a phase field model in 2D and 3D continua in homogeneous and heterogeneous materials. The phase field model for fracture has specific regulations regarding the finite element mesh size. Therefore, a mesh refinement algorithm by adopting a predictor-corrector mesh refinement strategy is used in both applications of mechanical and thermo-mechanical fracture models. Several mechanical and thermo-mechanical examples are presented in this work to prove the capability of the proposed numerical implementation. The multi-field problems are solved using a staggered solution algorithm with and without the parallelization of the system equations. The simulation times of the tested specimens are compared for different meshing criteria, adaptive refinement, pre-refinement of the expected crack path, and the global refinement of the specimen.

### 1. Introduction

Detection and tracking of thermally induced cracks are of great importance in engineering analysis and design. A major reason of failure in many engineering systems is the propagation of cracks in bodies due to transient loads applied to the boundary. Therefore, evaluating thermal induced cracks and following the mechanism of thermal fracture are required to improve the engineering materials properties. Different complicated cracks penetrate into the interior of the material from the surface when subjected to thermal shock. Many studies have stated these problems in the literature [1]. Furthermore, the spatial pattern of thermal produced cracks is very complicated to understand by traditional fracture mechanics. Accurate study of the global evaluation of cracks helps for more understanding of the behavior of thermally induced cracks.

The recently improved phase field methods to fracture are regularizing sharp crack discontinuities in continuum formulation. This crack surface functional model provides the interpretation of complicated failure topologies, such as crack propagation and branching in brittle solids. The phase field method as a spatially smooth continuum model that evades modeling of discontinuities can be performed by coupling multi-field finite element solvers. Likewise to phase field, Areias et al. [2] presented an enhanced gradient damage model with an additional

damage-related quantity as an additional field. This damage model combines the localization limiter in the form of the screened Poisson equation and local mesh refinement to capture the strain localization. In contrast to phase field approaches, the cracking particles method [3–5] and dual-horizon peridynamics [6,7] are considered as computationally chapter discrete fracture approaches, since they require a much coarser discretization and do not need to discretize another variable, i.e. the phase field.

The basis of phase field approaches for brittle fracture can be outlined by the classical Griffith criterion [8] which introduced the total energy functional as the sum of the fracture energy and elastic energy parts. The earlier significant additions to the phase field model formulations are sorted in Refs. [9–11]. The quasi-static brittle fracture of phase field and its applications have been developed by Bourdin et al. [12–14], Miehe et al. [15], Borden et al. [16], Meskh et al. [17], and Ambati et al. [18]. Furthermore, the phase field model is extended to different disciplines such as: shell structures [19–21], dynamic fracture [22,23], ductile fracture [24–26], hydraulic fracturing [27–31], multiphysics [32–35], and many others.

In the field of multiphysics, Miehe et al. [34] have postulated the phase field method towards a particular geometric account based on a constitutive evolution equation for the regularized crack surface. Accordingly, the stress-based constitutive driving forces can be incor-

\* Corresponding author.

\*\* Corresponding author.

E-mail addresses: [ha.badnava@me.iut.ac.ir](mailto:ha.badnava@me.iut.ac.ir) (H. Badnava), [mohammed.msekh@outlook.com](mailto:mohammed.msekh@outlook.com) (M.A. Msekh).

<sup>1</sup> Equal contribution.

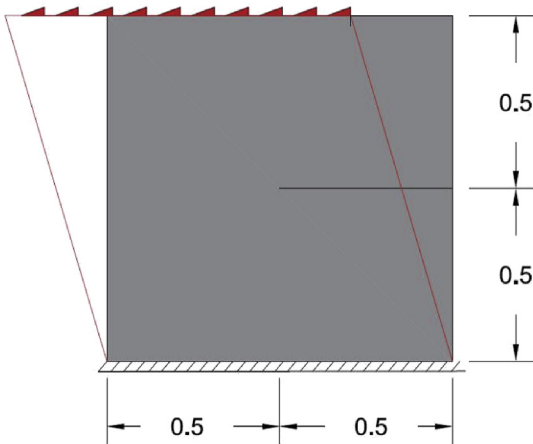


Fig. 1. Geometry and boundary conditions of single edge notch shear test.

porated, which allow for the phase field modeling in anisotropic and multiphysics problems. Coupling of the phase field model with complex multi-physics such as a thermo-elastic model generalizes the crack driving forces from the energetic criteria towards stress-based criteria. Conceptually, the constitutive modeling of heat conduction across cracks and convective heat exchanges at crack faces depending on new constitutive functions. This coupling can be achieved by approximating surface load integrals of the sharp crack approach by a special volume integrals.

Cracks propagation in the multi-phase material is of interesting application due to a different physical phenomenon that controls the composite material behavior and strength [36,37]. Of course, studying the cracks behavior in a composite material subjected to thermo-mechanical loading is a complex physical behavior. For example, in two-phase composite materials, the difference between coefficient of thermal expansion in matrix and reinforcement can cause micro-cracks. These effects have been investigated on the cement-based composite subjected to elevated temperatures by Fu et al. [38]. Their results revealed that the difference between coefficients of thermal expansion in matrix and reinforcement can lead to the change of the crack type at the interface and/or inside the matrix. Polymeric composite materials were similarly analyzed through an experimental investigation conducted by Hiemstra and Sottos [39]. They also reported similar results. Davidge and Green [40] investigated the effect of the matrix and reinforcement mechanical properties and the percentage of the reinforcement within the matrix on the produced stresses in the two-phase ceramic/glass composite material during a high temperature fabrication process.

The aim of this work is to investigate the application of the phase field model for thermo-mechanical fracture in 2D and 3D with and without mesh refinement. The influence of material thermal properties on cracks propagation is observed in composite specimens. While in homogeneous materials, we show the cracks induced by thermal shock and its impact on heat conduction through the specimen media. Furthermore, the computational cost, which is a predominant factor in the phase field method, is investigated for different meshes criteria.

The outline of this article is as following: Section 2 explains the numerical model formulation. Section 3 presents and discusses different application of the implemented model. The conclusion of the work is listed in Section 4.

## 2. Thermo-mechanical phase field model

The main idea of phase field is to evaluate the sharp discontinuity by a smeared surface  $\Gamma_l$ . Therefore, an auxiliary field, called order phase field variable is introduced to represent the crack. An infinite bar with

position  $\chi \in [-\infty, +\infty]$  of its axis with a crack at the axial position  $\chi = 0$  is considered. The sharp crack can be demonstrated using a scalar phase field as:

$$d = \begin{cases} 1 & \text{for } \chi = 0 \\ 0 & \text{otherwise} \end{cases}, \quad (1)$$

in which  $d$  is the phase field variable. In the other hand, the crack discontinuity is described by a scalar field  $d \in [0, 1]$  where the undamaged state characterizes by  $d = 0$  and the fully-cracked state of a material point is described by  $d = 1$ . The defined scalar field is similar to the damage mechanics concept. In one-dimensional phase field model, the sharp crack discontinuity can be approximated using the following exponential function.

$$d(x) = e^{-|x|/l}. \quad (2)$$

Note that, the equation above is the solution of the following differential equation ( $d - l^2 d_{xx} = 0$ ). In which the comma denotes the differentiation. As demonstrated by Miehe et al. [15], the crack surface can be approximated by  $\Gamma_l$  as follow:

$$\Gamma_l = \int_{\Omega} \gamma_l dV = \int_{\Omega} \frac{1}{2l} (d^2 + l^2 d_x^2) dV = 0, \quad (3)$$

in which the functional  $\gamma_l$  can be considered as the crack surface density and its expansion to a multi-dimensional case is,

$$\gamma_l := \frac{1}{2l} (d^2 + l^2 d_i d_i). \quad (4)$$

The three-dimensional form of Equation (4) is similar to the implicit gradient-enhanced damage model with different interpretations. The gradient based formulation is usually used to remove mesh sensitivity in finite element simulations [41,42]. However, this makes gradient-enhanced damage formulations less suitable to simulate a sharp crack [43]. The total energy functional can be written as,

$$E(\mathbf{u}, d) = \int_{\Omega} \Psi(\epsilon, d) dV = \int_{\Omega} G_c \gamma_l dV + \int_{\Omega} \Psi_0^{el} dV. \quad (5)$$

The first term is the fracture energy due to crack,  $G_c$  is the critical energy release rate, and the second term is the elastic energy. When the total energy is minimized with respect to the admissible phase field variable and displacement fields and under given boundary conditions, the regularized formulation of the crack evolution is determined. Using the assumption of isotropic degradation of stored bulk energy due to fracture; the elastic energy density is defined as,

$$\Psi^{el}(\epsilon, d) = [g(d) + k] \Psi_0^{el}(\epsilon), \quad (6)$$

$$\Psi_0^{el}(\epsilon) = \frac{1}{2} \epsilon : \mathbf{C}^e : \epsilon, \quad (7)$$

where  $g(d)$  is a degradation function.  $\Psi_0^{el}(\epsilon)$  is a standard elastic energy for undamaged solids, and  $\mathbf{C}^e$  is the fourth-order elastic stiffness tensor for undamaged material and equals to

$$\mathbf{C}^e = 2\mu \mathbf{I}_s + \lambda \mathbf{I} \otimes \mathbf{I} \quad (8)$$

$\lambda$  and  $\mu$  are Lame constants,  $\mathbf{I}$  is the second-order identity tensor and  $\mathbf{I}_s$  is the fourth-order symmetric identity tensor. The small positive dimensionless parameter  $0 < k \ll 1$  is a stabilizer parameters which is introduced to avoid numerical difficulties at fully damaged state  $d = 1$ . A small remaining elastic energy density  $k\Psi_0^{el}$  keeps the algebraic well-posed condition for the partly damaged material points. In Equation (6), the degradation function  $g(d)$  is a monotonically decreasing function and is used to reduce the material stiffness due to damage. The degradation function has the following properties,

$$\begin{cases} g(0) = 1 & \text{and } g(1) = 0 \\ g'(0) \neq 0 & \text{and } g'(1) = 0 \end{cases} \quad (9)$$

In this work a quadratic function that has the above properties is used,  $g(d) = (1 - d)^2$ . (10)

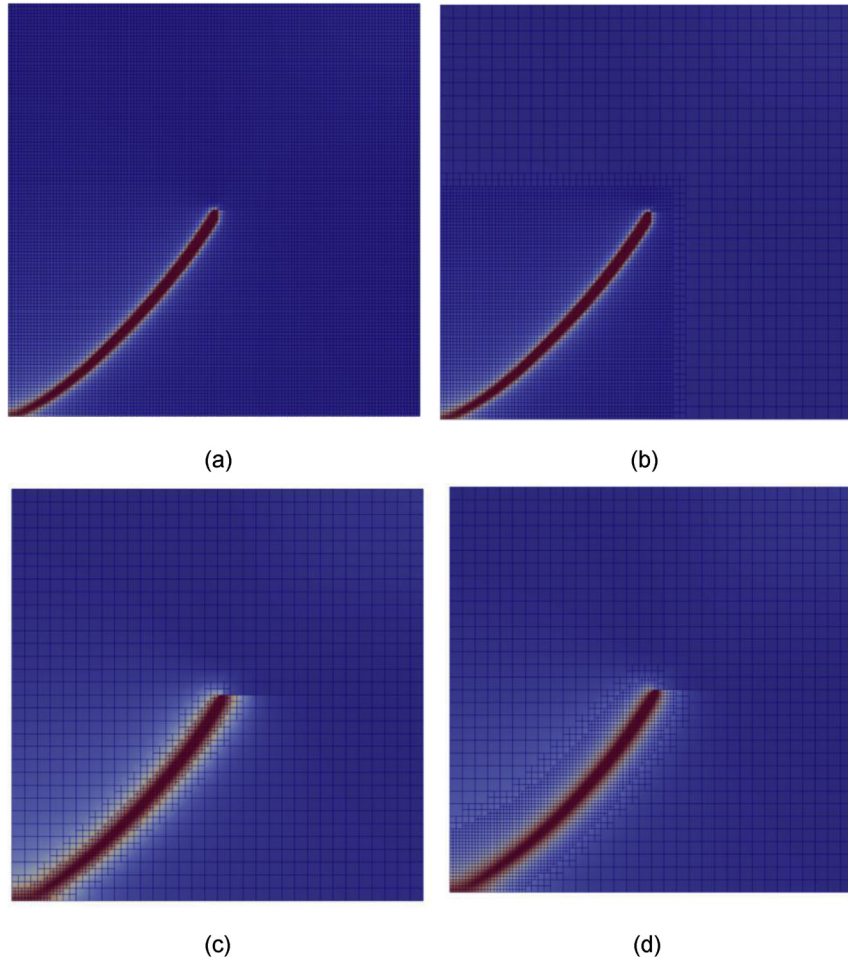


**Fig. 2.** Phase field contour for different mesh strategies. (a) Uniform mesh, (b) One quarter of the specimen is refined, (c) and (d) Meshed using the adopted mesh adaptivity scheme.

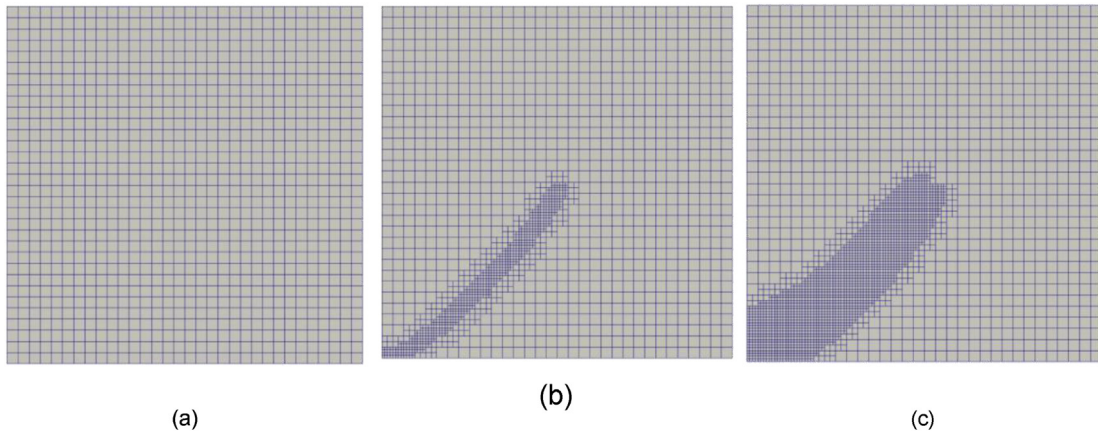


**Fig. 3.** 2D Shear test: (a) The initial coarse mesh, and the final mesh for (b) Limit 0.8, and (c) Limit 0.2.

The readers are referred to [15,17] for more details. By substituting Equations (6), (7) and (10) into the total energy functional 5, the latter can be rewritten as,

$$E(\mathbf{u}, d) = \int_{\Omega} G_c \gamma_l dV + \int_{\Omega} [(1-d)^2 + k] \Psi_0^{el}(\epsilon) dV. \quad (11)$$

The total energy functional  $E(u, d)$  must be minimized for a given equilibrium state,

$$\delta E(\mathbf{u}, d) = \frac{\partial E(\mathbf{u}, d)}{\partial \epsilon} \delta \epsilon + \frac{\partial E(\mathbf{u}, d)}{\partial d} \delta d + \frac{\partial E(\mathbf{u}, d)}{\partial \dot{d}} \delta \dot{d} = 0. \quad (12)$$

The regularized formulation of the crack propagation is determined using the minimization under given boundary conditions. For the minimization, the variation of total energy functional must be zero for all admissible values of  $\delta \epsilon$  and  $\delta d$ . According to this condition, the strong form of system equations for the displacement field and the phase field can be derived as,

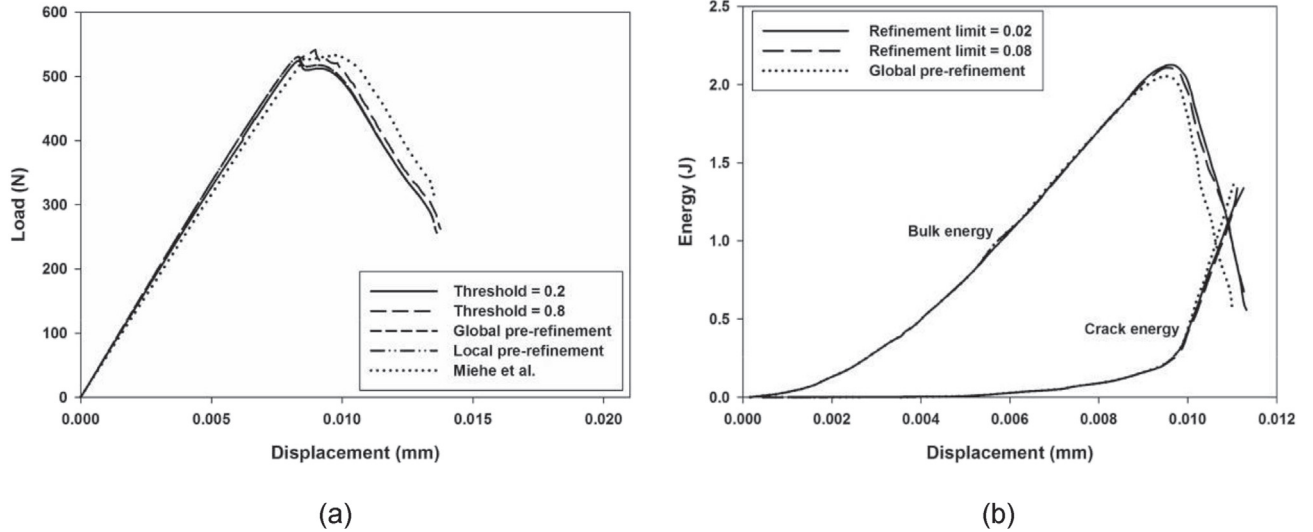


Fig. 4. 2D shear test. (a) Load-displacement curves for different prescribed temperatures, (b) bulk and crack energies.

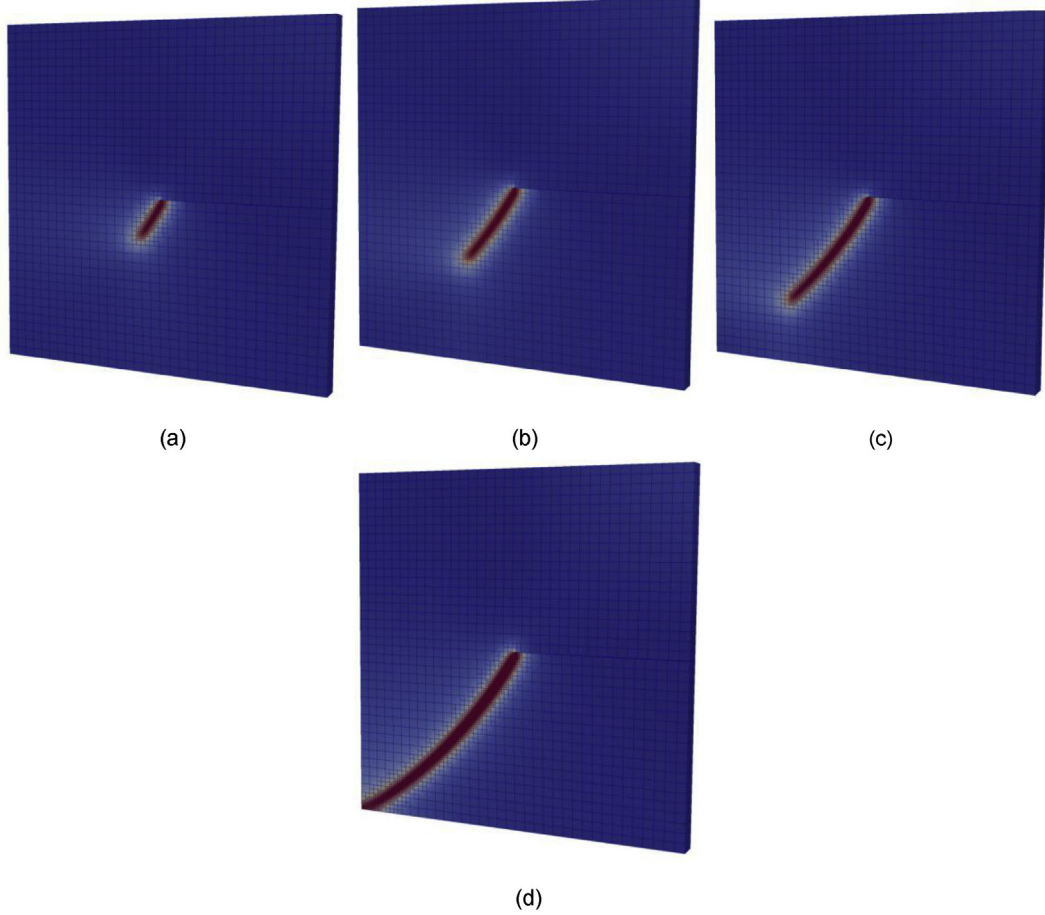


Fig. 5. 3D shear simulation: crack propagation at different time steps (a) 95 (b) 110 (c) 125 (d) 160.

$$\begin{cases} \nabla \cdot \sigma = 0 \\ \frac{G_c}{l}(d - l^2 \Delta d) = 2(1-d)\Psi_0^{el}(\epsilon) \end{cases}, \quad (13)$$

where  $\sigma$  is the so called Cauchy stress tensor. The above system of equations are subjected to the following boundary conditions,

$$\begin{cases} \sigma \cdot \mathbf{n} = \mathbf{t}_N & \text{at } \partial\Omega_t \\ \nabla d \cdot \mathbf{n} = 0 & \text{at } \partial\Omega \end{cases}, \quad (14)$$

in which  $\mathbf{n}$  is the unit normal vector to the surface and  $\mathbf{t}_N$  the surface traction vector. The constitutive equation for the stress is obtained as,

$$\sigma = \partial_\epsilon \Psi = \partial_\epsilon \Psi^{el} = [(1-d)^2 + k] \mathbf{C}^e : \epsilon \quad (15)$$

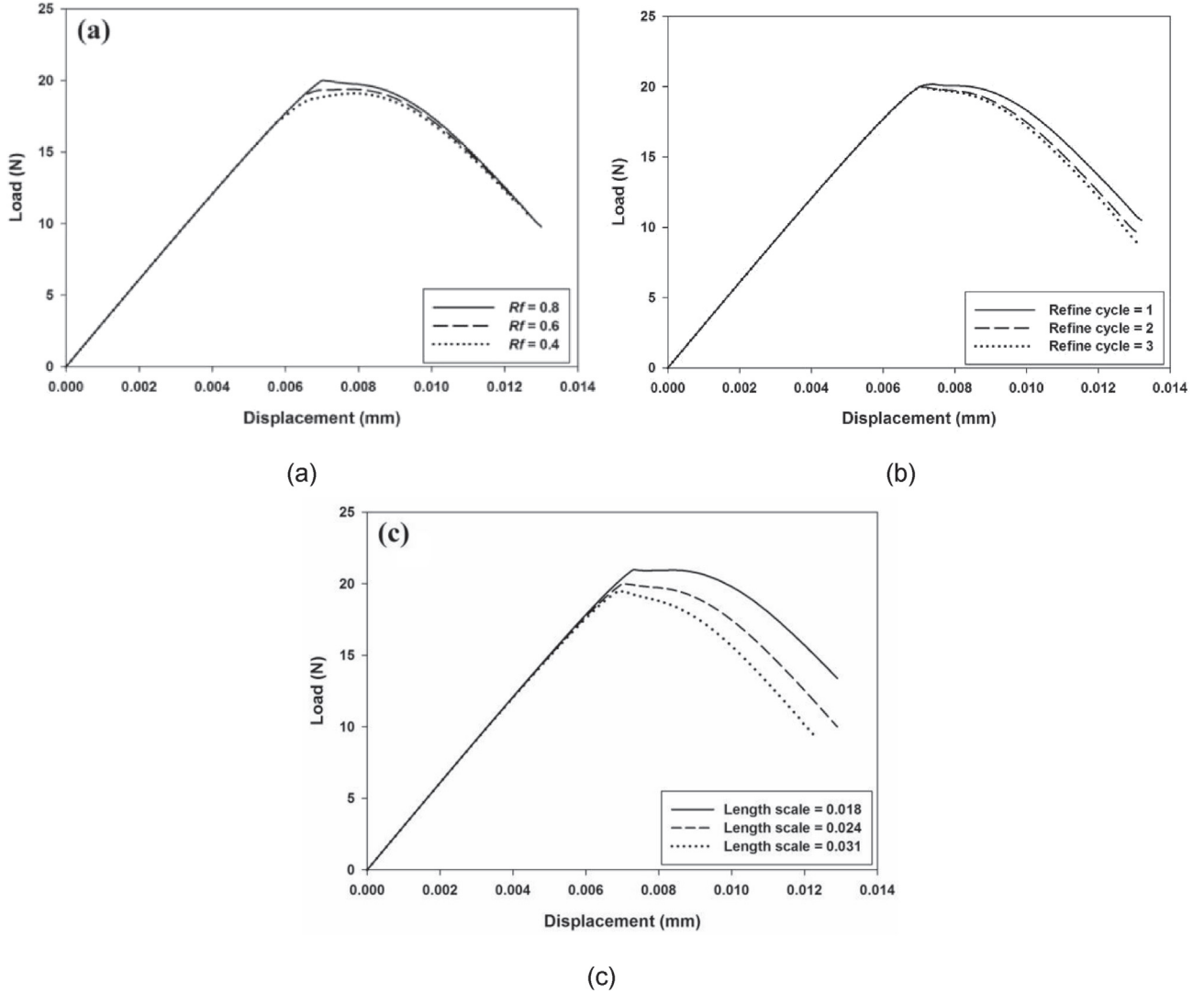


**Fig. 6.** Load-displacement curves for 3D shear tests. Effects of the (a) Adaptive refinement threshold for fixed  $l = 0.024$  mm and 2 refinement cycles, (b) Adaptive refinement cycle for fixed  $l = 0.024$  mm and refinement threshold  $R_f = 0.8$ , and (c) Length scale parameter for fixed refinement threshold  $R_f = 0.8$  and 2 refinement cycles.

The right hand side term in Equation (13) is the crack driving force. However, this definition leads to a reversible phase field formulation, in which the phase field variable is free to evolve based on the loading history. It means that cracks can disappear during unloading. In order to overcome this problem, the damage like formulation is used here. According to this, a history parameter is defined as,

$$H := \max(\Psi_0^{el}) \quad (16)$$

In the other hand, the history parameter satisfies the Kuhn-Tucker conditions for loading and unloading,

$$(\Psi_0^{el} - H) > 0, \quad H \geq 0 \quad \text{and} \quad H(\Psi_0^{el} - H) = 0, \quad (17)$$

substituting Equation (16) into Equation (13) yield to,

$$\frac{G_c}{l}(d - l^2 \Delta d) = 2(1 - d)H. \quad (18)$$

A primal-dual active set strategy has been proposed by Heister et al. [44] to enforce crack irreversibility as a constraint. An alternative approach has been suggested by Bourdin et al. [45], in which Dirichlet boundary conditions are imposed on the phase field variable.

Using the appropriate coupling between the phase field and the constitutive equations, the model can be utilized to a large range of

material models. The key term in developing the introduced phase field model to thermally induced brittle fracture is considering the effect of the thermal strain. The deformation of the material is due to mechanical loads and thermal effects. Consequently, in a small strain theory, the total strain is the sum of the elastic strain and the thermal strain.

$$\epsilon = \epsilon^e + \epsilon^{th}. \quad (19)$$

Only the elastic component of the total strain tensor contributes to the standard elastic energy function as well as into the phase field driving force. The elastic energy for undamaged solids is modified to,

$$\Psi_0^{el}(\epsilon^e) = \frac{1}{2}(\epsilon^e : C^e : \epsilon^e). \quad (20)$$

According to this definition, the stress is determined using the elastic strain,

$$\sigma = [(1 - d)^2 + k]C^e : \epsilon^e \quad (21)$$

The elastic strain is  $\epsilon^e = \epsilon - \epsilon^{th}$  and the constitutive equation can be rewritten as,

$$\sigma = [(1 - d)^2 + k]C^e : (\epsilon - \epsilon^{th}) \quad (22)$$

The mechanical part is a function of the mechanical load. The thermal part,  $\epsilon^{th}$ , depends on the coefficient of thermal expansion,  $\alpha$ . For

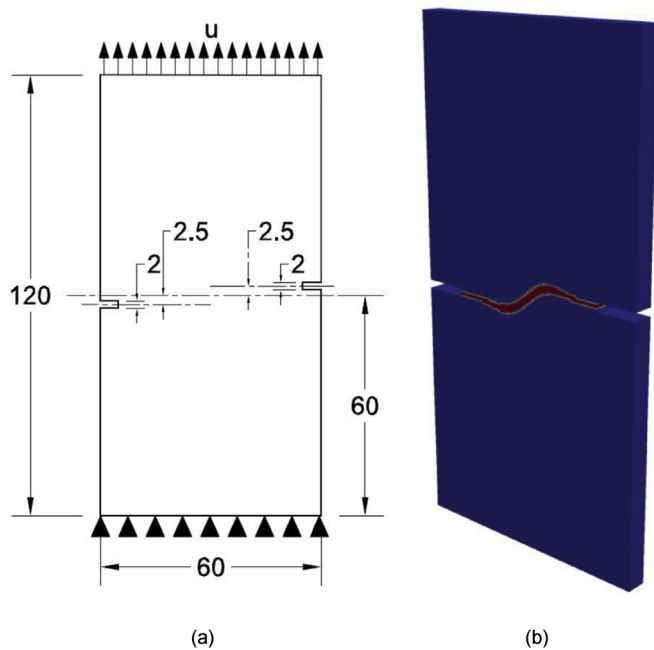


**Fig. 7.** 3D double-notched sample: (a) Geometry. Dimensions are in mm. (b) The final state of the phase field variable.

materials that expand isotropically, when the temperature is increased, the thermal part can be computed as,

$$\boldsymbol{\varepsilon}^{\text{th}} = \alpha(T - T_0)\mathbf{I}, \quad (23)$$

in which  $T_0$  is the initial temperature. Mechanical restraints on  $\boldsymbol{\varepsilon}$  or different coefficients of thermal expansion can restrict the isotropic expansion and result in a stress state.

The developed phase field fracture model does not distinguish between compressive and tensile load cases. However, it is obvious that the stiffness degradation due to the presence of micro-cracks and voids is much more considerable in tension than in compression. In order to account the stress degradation only in tension, the strain tensor is decomposed into positive and negative parts using a spectral decomposition method. Any strain tensor can be represented as a diagonal matrix with the diagonal terms contains the principal values. Using the principal values  $\varepsilon_i^e$  and the principal direction  $\mathbf{e}_i$ , the elastic strain tensor can be written as,

$$\boldsymbol{\varepsilon}^e = \sum_{i=0}^3 \varepsilon_i^e \mathbf{e}_i \otimes \mathbf{e}_i. \quad (24)$$

The positive/negative split of the elastic strain tensor consists in splitting additively as,

$$\boldsymbol{\varepsilon}^e = \boldsymbol{\varepsilon}_+^e + \boldsymbol{\varepsilon}_-^e, \quad (25)$$

in which  $\boldsymbol{\varepsilon}_+^e$  and  $\boldsymbol{\varepsilon}_-^e$  are the positive and negative parts of the elastic strain tensor, respectively and are defined as,

$$\begin{cases} \boldsymbol{\varepsilon}_+^e = \sum_{i=0}^3 \langle \varepsilon_i^e \rangle \mathbf{e}_i \otimes \mathbf{e}_i \\ \boldsymbol{\varepsilon}_-^e = -\sum_{i=0}^3 \langle -\varepsilon_i^e \rangle \mathbf{e}_i \otimes \mathbf{e}_i \end{cases}, \quad (26)$$

where  $\langle \cdot \rangle$  is the Macauley's bracket that is defined as:

$$\langle x \rangle := \begin{cases} x & \text{if } x \geq 0 \\ 0 & \text{if } x < 0 \end{cases}. \quad (27)$$

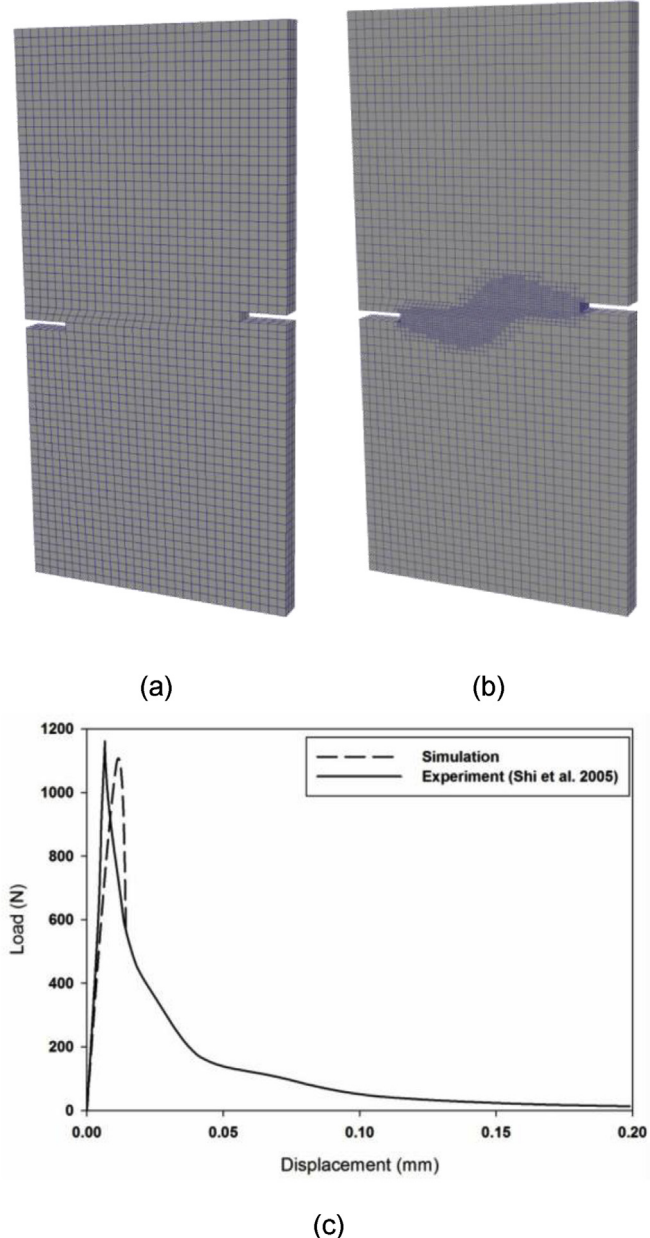


**Fig. 8.** 3D double-notched sample: (a) The initial mesh, (b) The final mesh, and (c) Reaction forces.

According to the above notation, the standard elastic energy function is additively decomposed to a positive part  $\Psi_0^{\text{el}+}$  due to tension and a negative part  $\Psi_0^{\text{el}-}$  due to compression as,

$$\Psi_0^{\text{el}} = \Psi_0^{\text{el}+} + \Psi_0^{\text{el}-}, \quad (28)$$

where,

$$\begin{cases} \Psi_0^{\text{el}+} = \frac{1}{2} \boldsymbol{\varepsilon}_+^e : \mathbf{C}^e : \boldsymbol{\varepsilon}_+^e \\ \Psi_0^{\text{el}-} = \frac{1}{2} \boldsymbol{\varepsilon}_-^e : \mathbf{C}^e : \boldsymbol{\varepsilon}_-^e \end{cases}. \quad (29)$$

The key term that leads to the crack evolution due to the tensile part is using the positive part  $\Psi_0^{\text{el}+}$  of the elastic energy in the history parameter definition as,

$$H := \max(\Psi_0^{\text{el}+}), \quad (30)$$

**Table 1**  
Composite 1 and composite 2 properties.

	Composite 1		Composite 2	
	Matrix	Reinforcement	Matrix	Reinforcement
Young modulus (GPa)	28.16	244.6	28.16	244.6
Poisson's ratio	0.2	0.275	0.2	0.275
Critical energy release rate (N/m)	200	400	100	105
Length scale/Mesh size	2.0	2.0	2.0	2.0
Density (kg/m <sup>3</sup> )	2700.0	2900.0	2700.0	2900.0
Thermal expansion (K <sup>-1</sup> )	$6.8 \times 10^{-6}$	$8.7 \times 10^{-6}$	$10.5 \times 10^{-6}$	$8.7 \times 10^{-6}$
Conduction coefficient (W/mK)	1200.0	1250.0	1200.0	1250.0
Convection coefficient (W/m <sup>2</sup> K)	150.0	150.0	150.0	150.0
Specific heat capacity (J/K)	530.0	550.0	530.0	550.0

the constitutive equation can be rewritten as,

$$\sigma = [(1-d)^2 + k] \frac{\partial \Psi_0^{el+}}{\partial \epsilon} + \frac{\partial \Psi_0^{el-}}{\partial \epsilon} \quad (31)$$

### 2.1. Thermal effect

In order to take into account the thermal effects into the phase field, the temperature field must be determined. Hence, in addition to the mechanical equilibrium Equation (13) and the phase field evolution Equation (18), the energy balance equation needs to be solved. Considering the heat flow equilibrium in the body interior, the strong form of the energy balance equation is given as follows,

$$k\nabla \cdot (\nabla T) - \rho C_p \dot{T} + \underset{Gen}{\dot{q}} = 0, \quad (32)$$

where  $C_p$  is the heat capacity,  $k$  the thermal conductivity,  $T$  the temperature, and  $\dot{q}$  the rate of heat generation by material per unit volume. Equation (32) describes the thermal conduction process. Convective and radiative heat transfer with the environment depend on a set of boundary conditions. On the surface of the body, the following boundary conditions must be satisfied,

$$\begin{cases} T = T_s & \text{on } \partial\Omega_T \\ -k\nabla T \cdot \mathbf{n} = q_s & \text{on } \partial\Omega_q \end{cases}, \quad (33)$$

in which  $T_s$  is the known surface temperature on  $\partial\Omega_T$ , and  $q_s$  is the prescribed heat flux on the surface  $\partial\Omega_q$ .

**Table 2**  
Corner crack specimen properties.

Young modulus (MPa)	210.0
Poisson's ratio	0.3
Critical energy release rate (N/m)	7700
Length scale/Mesh size	2.0
Density (kg/m <sup>3</sup> )	2600.0
Conduction coefficient (W/mK)	950.0
Specific heat capacity (J/K)	500.0

**Table 3**  
Specimen properties.

Young modulus (GPa)	201.6
Poisson's ratio	0.25
Critical energy release rate (N/m)	200
Length scale/Mesh size	1.5
Density (kg/m <sup>3</sup> )	2800.0
Thermal expansion (K <sup>-1</sup> )	$2.8 \times 10^{-5}$
Conduction coefficient (W/mK)	900.0
Specific heat capacity (J/K)	660.0

### 2.2. Finite element implementation

The finite element implementation of the initial boundary value problem is explained in this section. The starting point for the finite element implementation is converting the strong forms of the displacement equilibrium Equation (13) and the phase field system Equation (18) to weak forms. By integration the displacement equilibrium Equation (13) over the domain:

$$\int_{\Omega} \delta \mathbf{u} \cdot (\nabla \cdot \sigma) = 0. \quad (34)$$

By applying the divergence theorem and using the chain rule, in addition, by applying the boundary Equation (14), Equation (34) can be transferred to,

$$\int_{\Omega} (\nabla \delta \mathbf{u})^T : \sigma dV = \int_{\partial\Omega} (\delta \mathbf{u})^T \mathbf{t}_N dS. \quad (35)$$

Using the same method as described for the previous field, multiplication of the strong form of the phase field Equation (18) by  $\delta d$  followed by integration over the volume leads to,

$$\int_{\Omega} \delta d \left\{ \frac{G_c}{l} (d - l^2 \Delta d) - 2(1-d)H \right\} dV = 0. \quad (36)$$

Using the boundary conditions (Equation (14)) and the same approach as before, weak form of the phase field evaluation equation is obtained:

$$\int_{\partial\Omega} \left\{ \frac{G_c}{l} (\delta d d + (\nabla \delta d)^T \nabla d) - 2\delta d(1-d)H \right\} dV = 0. \quad (37)$$

By integration over the domain,

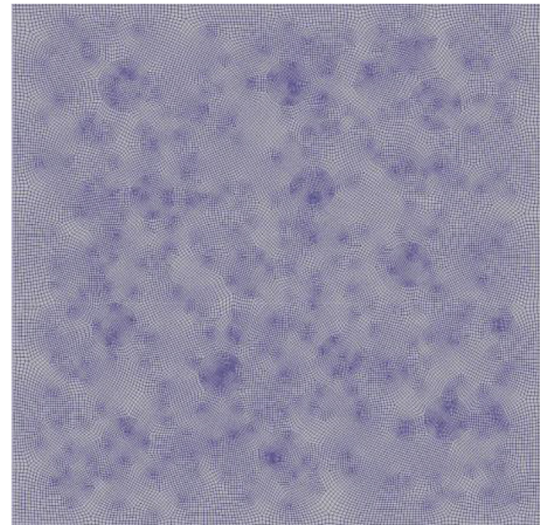


**Fig. 9.** Initial refined finite element discretization for the two-phase composite simulation without adaptive refinement.

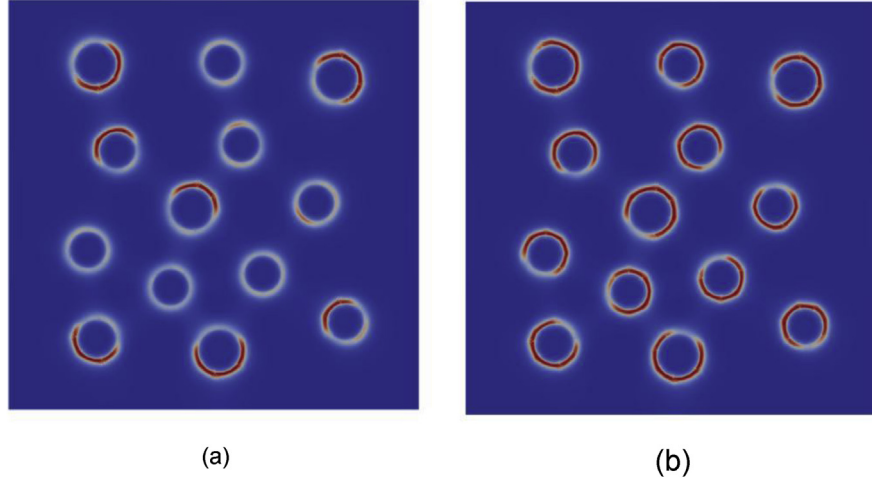


Fig. 10. Composite 1: phase field value without adaptive refinement at different thermal loading stages.

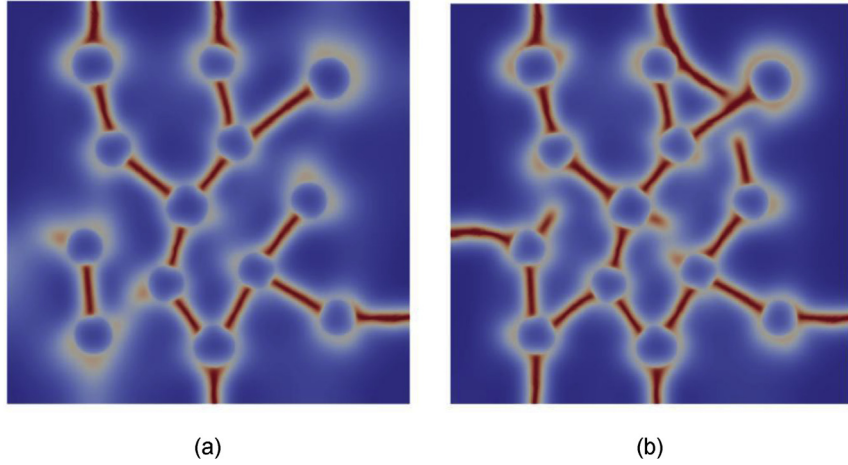


Fig. 11. Composite 2: phase field value without adaptive refinement.

$$\mathbf{u} = \mathbf{N}_u \mathbf{u}^e, \quad \delta \mathbf{u} = \mathbf{N}_u \mathbf{u}^e, \quad \boldsymbol{\varepsilon} = \mathbf{B}_u \mathbf{u}^e. \quad (38)$$

$$\mathbf{T} = \mathbf{N}_T \mathbf{T}^e, \quad \delta \mathbf{T} = \mathbf{N}_T \mathbf{T}^e, \quad \nabla \mathbf{T}^e = \mathbf{B}_T \mathbf{T}^e. \quad (39)$$

$$\mathbf{d} = \mathbf{N}_d \mathbf{d}^e, \quad \delta \mathbf{d} = \mathbf{N}_d \mathbf{d}^e, \quad \nabla \mathbf{d} = \mathbf{B}_d \mathbf{d}^e, \quad (40)$$

where  $\mathbf{N}_u$ ,  $\mathbf{N}_T$  and  $\mathbf{N}_d$  are the shape function matrices for the displacement field, temperature field and phase field, and  $\mathbf{B}_u$ ,  $\mathbf{B}_T$  and  $\mathbf{B}_d$  are matrices containing derivatives of the shape functions  $\mathbf{N}_u$ ,  $\mathbf{N}_T$  and  $\mathbf{N}_d$ , respectively. By substituting the above discretization relations into the three-field system given by Equations (35), (37) and (38) and after some modifications the relations will change to,

$$(\delta \mathbf{u})^T \underbrace{\int_{\Omega} \mathbf{B}_u^T \mathbf{D}^{ed} \mathbf{B}_u \mathbf{u} dV}_{f_{int}^u} - (\delta \mathbf{u})^T \underbrace{\int_{\partial\Omega} \mathbf{N}_u^T \mathbf{t}_N dS}_{f_{ext}^u} = 0. \quad (41)$$

$$(\delta \mathbf{d})^T \left[ \underbrace{\int_{\Omega} \left( \frac{\tilde{G}_c}{l} (\mathbf{N}_d^T \mathbf{N}_d + \mathbf{B}_d^T l^2 \mathbf{B}_d) \mathbf{d}^e - 2 \mathbf{N}_d^T (1-d) H \right) dV}_{f_{int}^d} \right] = 0. \quad (42)$$

$$(\delta \mathbf{T})^T \underbrace{\left[ \int_{\partial\Omega} \mathbf{N}_T^T q_s dS + \int_{\Omega} \mathbf{B}_T^T k \mathbf{B}_T \mathbf{T}^e dV + \int_{\Omega} \mathbf{N}_T^T f(T) dV - \int_{\Omega} \mathbf{N}_T^T \dot{q}_{Gen} dV \right]}_{f^T} = 0, \quad (43)$$

where  $\mathbf{D}^{ed} := d\sigma/d\varepsilon$  is the tangent matrix that is a combination of the damaged and undamaged parts of the elasticity matrix. The computation of the consistent tangent operator for the model is explained in Appendix A. The system of equations can be shown as follow,

$$\begin{bmatrix} \mathbf{f}_{int}^u - \mathbf{f}_{ext}^u \\ \mathbf{f}_{int}^d \\ \mathbf{f}^T \end{bmatrix} = 0 \quad (44)$$

### 2.3. Staggered solution

An operator split algorithm within the finite time step  $[t_n, t_{n+1}]$  is utilized to allow the staggered update of the temperature field, the phase field, and the displacement field [13,14,23,46–49]. It is also assumed that all field variables at the start of the time interval  $t_n$  are known and their values at time  $t_{n+1}$  must be determined. For each field, solution is obtained for increments of the primary fields from the iteration number  $i$  to  $i+1$  in the Newton-Raphson incremental iterative method. At the first step, the displacement and temperature fields are kept constant and the phase field is solved. The key term is to approximate the history variable based on the field variables at time  $t_n$ . Then, the phase field solution can be determined as,

$$\mathbf{d}_{i+1} = \mathbf{d}_i - (\mathbf{K}_d^{-1})_i (f_{int}^d)_i \quad (45)$$

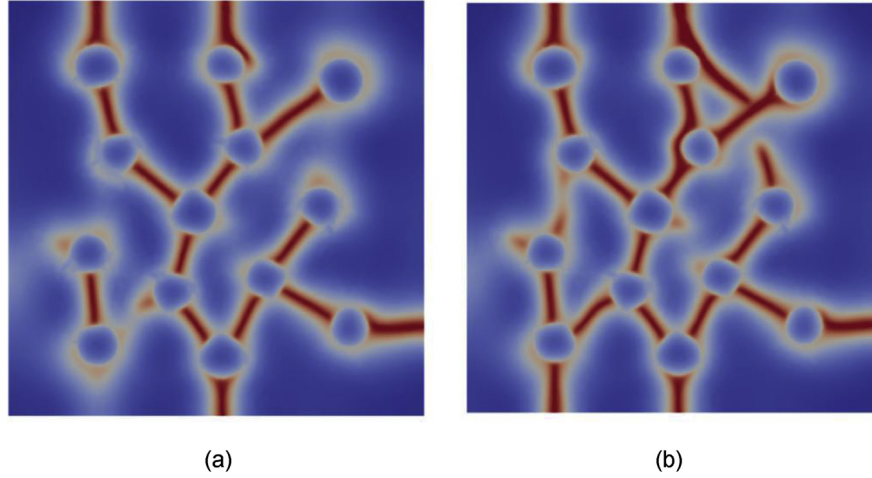


**Fig. 12.** Composite 2: phase field value obtained with adaptive refinement.

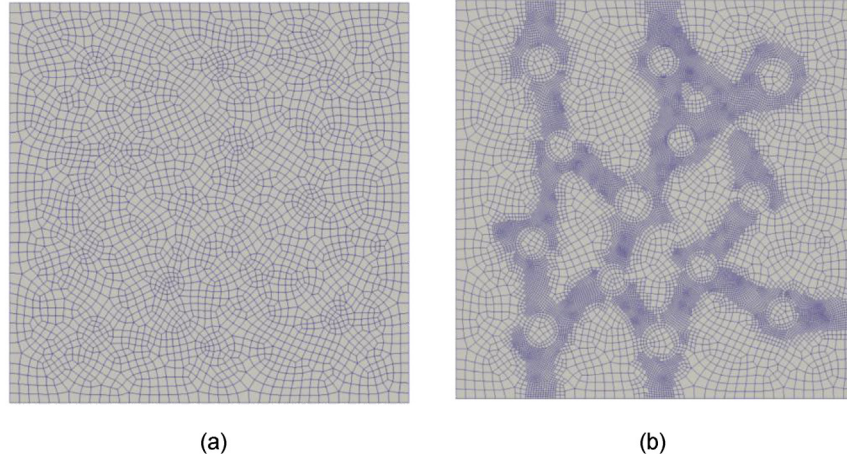


**Fig. 13.** Composite 2: mesh evolution during adaptive refinement, (a) Initial, and (b) Final mesh.

$$\mathbf{K}_d = \frac{\partial f_{\text{int}}^d}{\partial d} = \int_{\Omega} \left\{ \frac{G_c}{l} (\mathbf{N}_d^T \mathbf{N}_d + \mathbf{B}_d^T l^2 \mathbf{B}_d) d + 2 \mathbf{N}_d^T \mathbf{N}_d H \right\} dV. \quad (46)$$

After the fracture phase field has been determined the heat equation is solved for constant displacement and phase field.

$$\mathbf{T}_{i+1} = \mathbf{T}_i - (\mathbf{K}_T^{-1})_i (f^T)_i \quad (47)$$

$$\begin{aligned} \mathbf{K}_T = \frac{\partial f^T}{\partial T} &= \int_{\partial\Omega} \mathbf{N}_T^T h \mathbf{N}_T dS + \int_{\Omega} \mathbf{B}_T^T \mathbf{k} \mathbf{B}_T dV \\ &+ \int_{\Omega} \mathbf{N}_T^T \left( \frac{\partial f(T)}{\partial T} - \frac{\partial q_{\text{Gen}}}{\partial T} \right) \mathbf{N}_T dV. \end{aligned} \quad (48)$$

Note that, the backward difference method is utilized for the energy balance equation,

$$f(T) = \rho C_p (T_{n+1} - T_n) / \Delta t, \quad (49)$$

where  $\Delta t = t_{n+1} - t_n$  is the time increment. Finally, the displacement field updated as,

$$\mathbf{u}_{i+1} = \mathbf{u}_i - (\mathbf{K}_u^{-1})_i (f_u^i)_i \quad (50)$$

$$\mathbf{K}_u = \frac{\partial f_u^i}{\partial u} = \int_{\Omega} \mathbf{B}_u^T \mathbf{D}^{ed} \mathbf{B}_u dV \quad (51)$$

The staggered method is robust and provides flexibility in the solution algorithm (implicit or explicit methods). When the crack initiates, the time increment needs to be small enough to accurately simulate the propagation of the crack which degrades the computational efficiency.

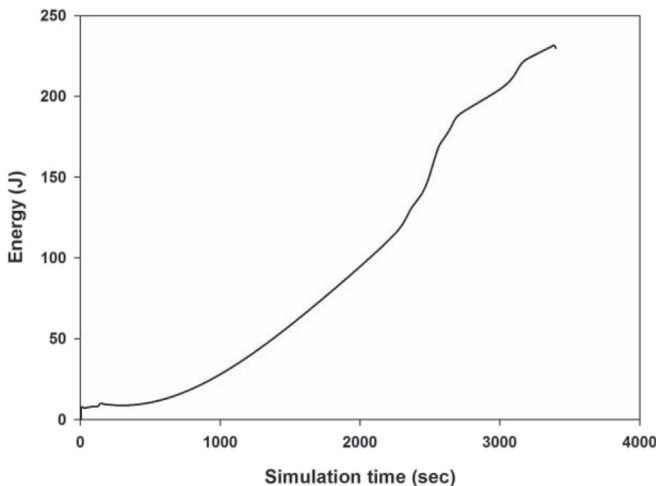


**Fig. 14.** Composite 2: Crack energy.

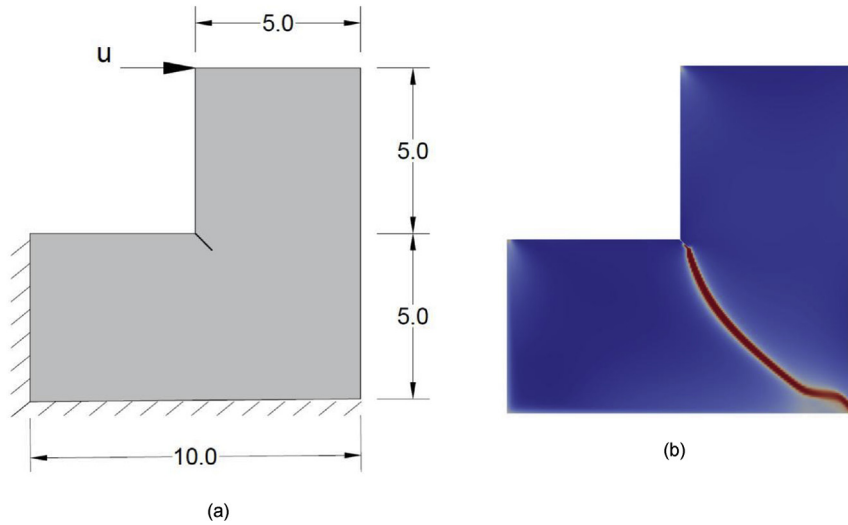


Fig. 15. (a) Corner crack sample: geometry and boundary conditions. (b) Final state of the phase field variable.

#### 2.4. Mesh adaptivity

It is well known that the phase field fracture model needs very fine mesh in order to provide an accurate solution. Hence, in most of the investigations, globally refined meshes have been used which sharply increase the computational cost [50,51]. Local mesh pre-refinement is also a well-known technique when the crack/damage path is known a priori [11,41,42]. However, in fracture propagation the path of the crack path is unknown. An adaptive mesh refinement method is used to develop a general technique in which no a priori information of the crack path is required. The challenging issue is that the crack must grow into regions with fine mesh. In order to overcome this challenge, a predictor-corrector scheme for mesh adaptively proposed by Ref. [44] is used here. At the first step, the system is solved to predict the crack path. After that, the mesh is refined based on the pre-specified refinement threshold. On each cell, the refinement flag is activated when the phase field value reaches to a predefined threshold [44,49]. Finally, the system is solved again for the previous time increment but on the refined mesh. The predictor-corrector mesh refinement process is continued in each time increment until the mesh does not change anymore.

### 3. Numerical results

In this section, we illustrate the performance of the proposed crack phase field model applied to the thermo-mechanical fracture numerical simulations. Each simulation aims to evaluate the capability of the model to predict crack nucleation and propagation in different loading conditions. Multiple cracks nucleation, propagation, branching and kinking can be demonstrated, especially in thermo-mechanical conditions. Moreover, the influence of the proposed adaptive refinement method on crack propagation and solution time is investigated. The developed finite element code is based on deal.II open source code [52,53].

#### 3.1. Mechanical problems with mesh refinement

##### 3.1.1. 2D mechanical test

The simulation of this benchmark can well predict the accuracy and precision of the proposed model and its numerical solution. Fig. 1 shows the geometry and boundary condition of the specimen. The results of the simulation depend on the samples and applied boundary conditions. The spectral decomposition is necessary in this example since it is Mode II fracture test. The maximum displacement is considered to be 0.02 mm

which is applied on 2000 increments of the solution so that the time of each increment is small enough. Furthermore, three different types of finite element discretization are used to demonstrate the influence of the adaptive h-refinement on crack propagation so as to compare it with the reference case in which the size of the element is small. In all three types, the structured quadrilateral elements are used. For the first type (Fig. 2a) of the meshing structure, 16384 elements were generated with size of  $h = 0.0027$  mm in all parts of the specimen. Moreover, the length scale  $l = 0.0055$  mm is considered for this model. For the second type (Fig. 2b), just one fourth of the specimen (the left bottom part), in which crack propagates, is meshed by  $h = 0.0027$  mm element size. For the other part of the specimen (Fig. 2c), the elements size is  $h = 0.011$  mm. For this type of meshing structure, 5995 elements were generated. For the third type, the adaptive h-refinement was used in which initial elements are not required to be necessarily small. Hence, the specimen is meshed with 1024 structured elements with the size of  $h = 0.011$  mm, while  $l = 2h$  as shown in Fig. 3. For simulations in which meshing structure changes automatically, length scale is computed for every change of the elements sizes. For each computation, the smallest size of elements is considered for computation. For each simulation in which the adaptive refinement is applied, the criterion of mesh changing is the phase field fracture variable. In the other word, if this variable at integration points of an element meets a determined value, the element changes through the mesh refinement process. To evaluate the influence of the mentioned parameter on the mesh refinement process and the phase field variable,  $Rf = 0.2$  and  $Rf = 0.8$  are considered in Fig. 2c and d, respectively. For these simulations the elastic modulus ( $E$ ) of 210 GPa, Poissons ratio  $\nu$  of 0.3 and the critical energy release rate ( $G_c$ ) of  $2.710^{-3}$  kN/mm are used.

For the mentioned specimens, the final distribution of the phase field fracture variable is demonstrated in Fig. 2. Comparing the distribution of the phase field with the results of the corresponding specimens reported by Miehe et al. verifies the accuracy of the simulation and numerical solution. Moreover, there is a good agreement between specimens with initial small elements (pre-refinement) and those in which adaptive refinement was used. It means that the predictor/corrector mesh refinement method can appropriately keep elements small at the area of crack propagation and the path of the crack has a good agreement with the outcomes obtained from the simulations without refinement. In addition, when  $Rf = 0.2$ , logically, larger area around the crack is refined, due to the fact that a smaller limitation means more elements have met the criterion of the refinement. In Fig. 3, the final meshing structure of two simulations with  $Rf = 0.2$  and  $Rf = 0.8$  are compared

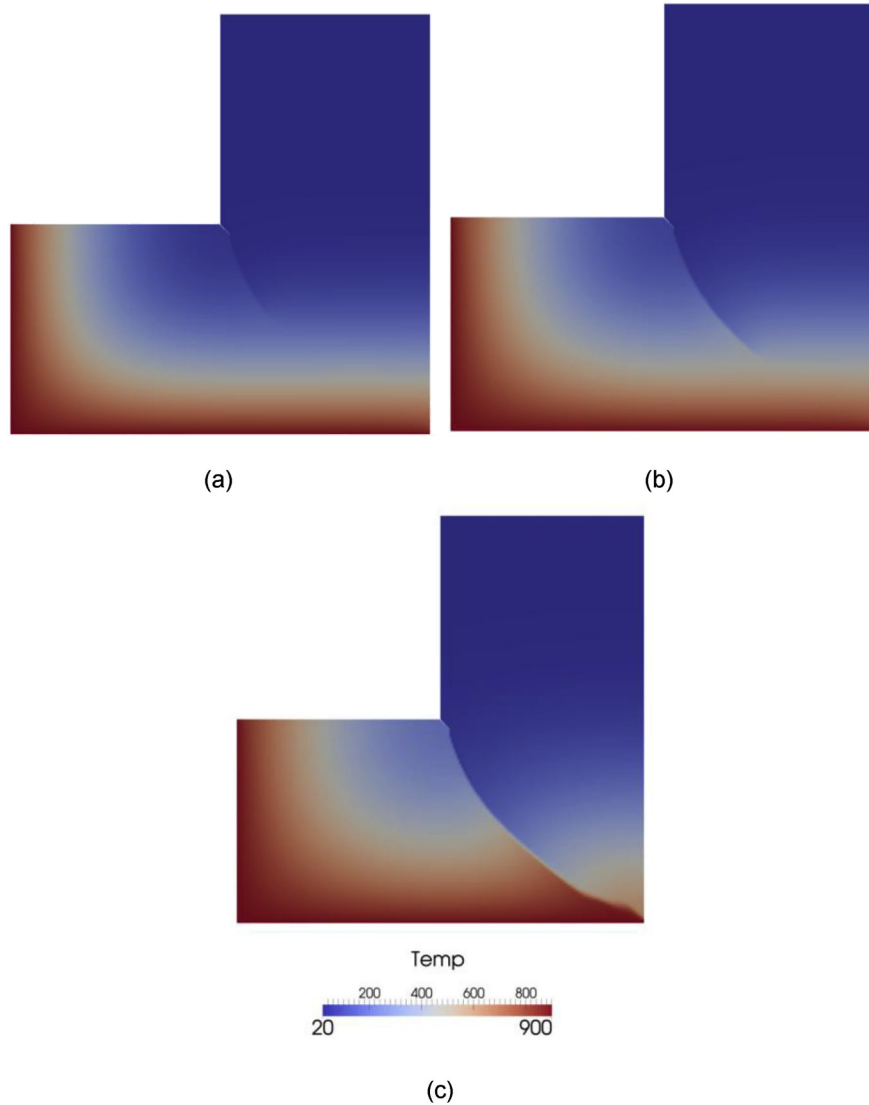


**Fig. 16.** (a–c) Temperature distribution at different times  $t = 2500$  s;  $3250$  s;  $4000$  s.

with the initial meshing structure. It can be understood that in this method, elements are just refined within the required area. The refined region is more concentrated around the crack when using  $Rf = 0.8$ . In Fig. 4a, the corresponding force-displacement curves are compared. The presented results verify the accuracy of the proposed phase field model and the process of the predictor/corrector mesh refinement. In addition, evolution of the bulk and crack energies for different refinement and global pre-refinement are compared in Fig. 4b. According to this, spatial convergence can be clearly observed.

### 3.1.2. 3D shear test

In order to demonstrate the ability of the phase field model to predict crack propagation in 3D case, the standard pure shear test is simulated here. The material parameters are  $E = 210$  GPa,  $\mu = 0.3$ , and  $G_c = 2.7$  N/mm. The threshold for the mesh refinement process,  $Rf = 0.6$ , is used for this simulation. The sample is initially discretized with 2770 uniform linear hexahedral elements and the length scale is equal to 0.016 mm. The time step,  $\Delta t = 1 \times 10^{-4}$  s is used and the displacement increment at each time step is considered to be 0.001 mm. Fig. 5 shows the crack patterns and corresponding mesh produced through predictor/corrector dynamic mesh refinement at different time steps. The obtained results are in good qualitative agreement with the

available results for the shear test. Another purpose is to study effects of the number of h-refinement cycles, the refinement threshold and the length scale parameter. Therefore, for the first case, these simulations are performed on different mesh refinement thresholds  $Rf = 0.8$ ,  $Rf = 0.6$  and  $Rf = 0.4$  for fixed  $l = 0.024$  mm and 2 refinement cycles. For the second case, these simulations are performed on different mesh refinement cycles 1, 2 and 3 for fixed  $l = 0.024$  mm and refinement threshold  $Rf = 0.8$ . For the third case, these simulations are performed on different length scales  $l = 0.018$  mm,  $l = 0.024$  mm and  $l = 0.031$  mm for fixed refinement threshold  $Rf = 0.8$  and 2 refinement cycles. The load-displacement curves obtained for these cases are shown in Fig. 6. For the first case, which its results is displayed in Fig. 6a, it is obvious that the results are almost identical. The largest differences are observed at the peak loads. The mesh density analysis helps to decide how refined mesh should be used in analysis to obtain accurate results. The influence of different mesh refinement cycles shown in Fig. 6b. It is obvious that spatial convergence with respect to h is obtained. Constant mesh refinement cycles with different length scales show the influence of the crack length scale on the results (Fig. 6c). Decreasing the length scale leads to an increase of the reaction force. This behavior is well known in the phase field model with a single crack propagating in the sample [15].

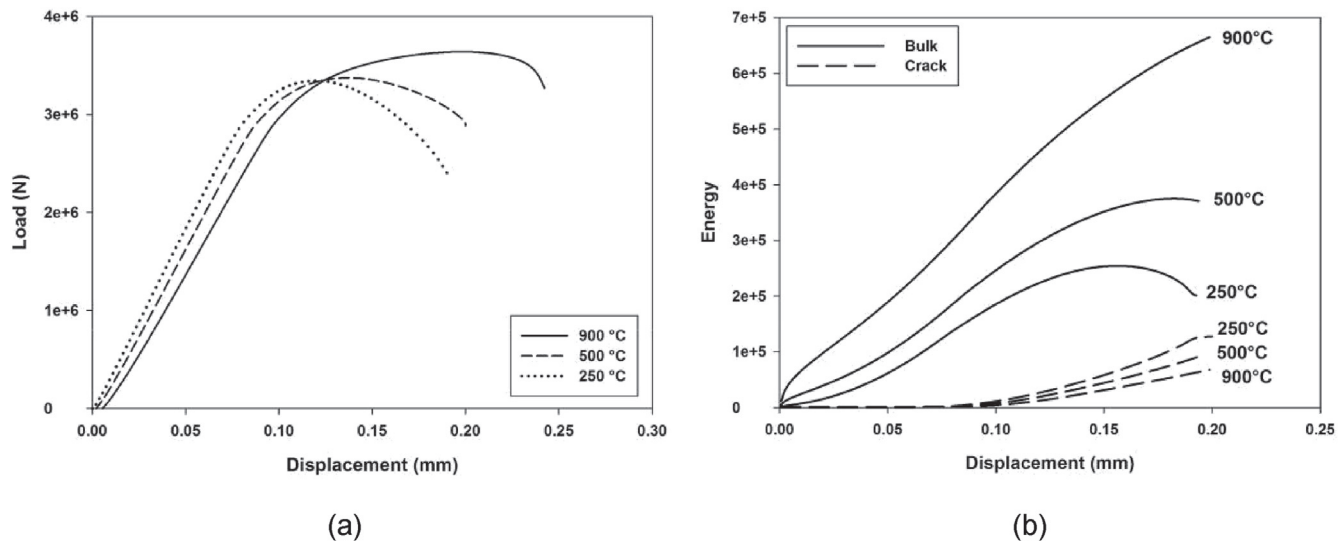


Fig. 17. Corner crack sample. (a) Load-displacement curves for different prescribed temperatures, (b) crack and bulk energies.

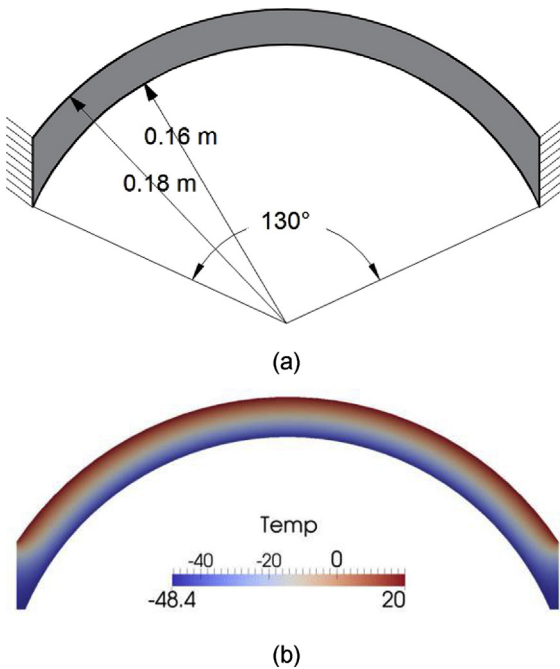


Fig. 18. Arc sample: (a) Geometry (b) Temperature distribution after 82 s.

### 3.1.3. 3D double notched sample

The double-notched sample under tension is considered to examine results of the proposed phase field model [54,55]. In this test, a double-notched sample is subjected to an axial tensile load (Fig. 7a). The vertical distance between the two notches is 5 mm. For this simulation, the model parameters are set to  $E = 30 \text{ GPa}$ ,  $\mu = 0.2$ ,  $G_c = 4.5 \text{ N/m}$ . The evolution of the phase field in the specimen is demonstrated in Fig. 7b in order to illustrate the crack path. This simulation was performed with adaptive refinement technique to demonstrate the ability of the proposed predictor/corrector mesh refinement for three-dimensional simulations. Fig. 8 demonstrates the initial coarse mesh and the final mesh after solution and applying the h-refinement technique. Initially 6105 elements are generated with size  $h = 4.3 \text{ mm}$  in all parts of the specimen. The final number of elements achieved after the adaptive refinement process, is 23451 with a mesh size  $h = 1.08 \text{ mm}$  at the refined

area with length scale parameter  $l = 2 \text{ h}$ . Fig. 8c depicts the resulting load-displacement curves for the developed phase field model and the experiment. The numerically obtained reaction load and crack path are similar to the corresponding experimental ones. The comparison between available experimental and numerical results shows the model ability to replicate the test results of brittle materials.

### 3.2. Thermo-mechanical problems with mesh refinement

The thermo-mechanical model is used here to simulate the process of the crack propagation in presence of the thermal influences. This section presents different numerical examples for different purposes. First, two simulations of composite materials are proposed in which the material is created by temperature variations. Second, a simulation is developed to investigate the effect of the thermal shock on the crack propagation in brittle materials. Third, a simulation is developed to show the effect of the crack on heat conduction. The model parameters for the following thermo-mechanical simulations are given in a table for each example (Tables 1–3).

#### 3.2.1. Thermal induced cracks in composite samples with mesh refinement

In this section, the initiation of the crack in a two-phase composite is investigated. In this composite, the matrix is a ceramic material reinforced by 10% of the volume by glass material. The test is cooling the specimen through the fabrication process. The cooling process can lead to crack initiation at the contact area of the matrix and spherical reinforcement. The reason of such a crack initiation is the different coefficients of thermal expansion of the matrix and reinforcement. Hence, two types of simulations can be developed for which the coefficient of thermal expansion of reinforcement is  $8.7 \times 10^{-6}$ . In the first case, the coefficient of thermal expansion of the matrix is  $6.8 \times 10^{-6}$  which is smaller than that of the reinforcement. For the second case, the thermal expansion coefficient for the matrix selected higher than the reinforcement coefficient and equals to  $10.5 \times 10^{-6}$ . The initial temperature of all points of the specimen is  $700^\circ\text{C}$  produced through the fabrication process. Afterward, the cooling process has accomplished, due to the heat convection in all the external boundaries of the specimen. In both simulations quadrilateral elements are used. For composite 1, adaptive refinement is not applied on the model, but the size of the elements was chosen small enough (global pre-refinement), at the beginning of the simulation. According to this procedure, the size of the elements is  $h = 0.0021 \text{ mm}$  and the number of the elements and degree of freedom

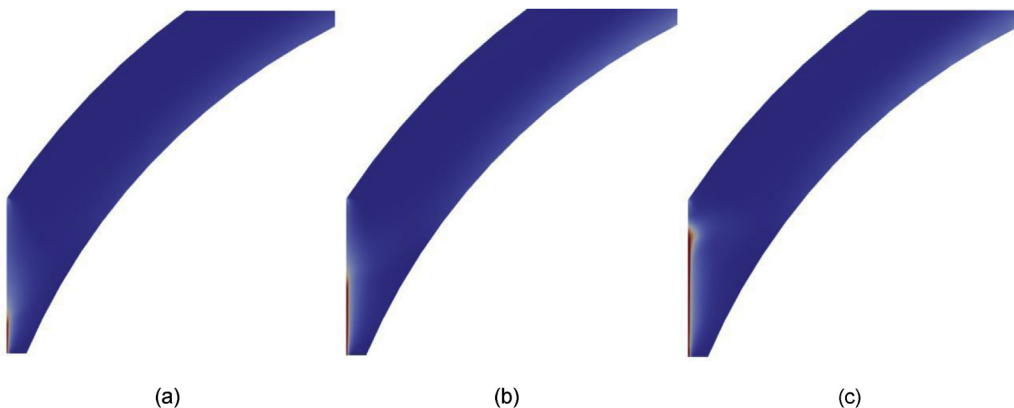


**Fig. 19.** Crack evolution at the end of the sample at different times (a)  $t = 2500$  s; (b)  $t = 3250$  s; (c)  $t = 4000$  s (tensile stress is produced due to cooling and sample contraction).

are 47808 and 192516, respectively (Fig. 9). The coefficients  $l$  and  $k$  are 0.0031 mm and  $2.1 \times 10^{-10}$  mm, respectively. In sample composite 2, the influence of the adaptive refinement is investigated.

In composite 1, the contraction of the spherical reinforcements is larger than that of matrix. Accordingly, reinforcements have positive stresses. Hence, the critical points are the boundaries between matrix and reinforcements. Fig. 10 shows two stages of the simulation in which cracks propagate around the reinforcements.

In composite 2, cracks propagate in matrix, due to the larger tensile stresses in matrix caused by larger contraction in matrix comparing with reinforcements. This simulation was also developed with and without adaptive refinement technique to evaluate the influence of the mesh refinement process in a thermo-mechanical loading condition. Figs. 11 and 12 show the distribution of the phase field variable at two different times of the cooling process for the specimens without and with adaptive refinement, respectively. At low temperatures, it is apparent that cracks are getting together torn the composite material to separate pieces. Fig. 13 demonstrates the initial coarse mesh and the final mesh after solution and applying the h-refinement technique. According to the outcomes, it can be understood that there is an insignificant difference between distributions of phase field variable in two simulations. It can be concluded that the pattern of the crack is depended to the properties of the composite material (the coefficients of thermal expansion of matrix and reinforcement). In the first case, micro-cracks are initiated around the reinforcements in a circumferential shape. While, in

the second case, cracks nucleate in the interfaces and propagate within the matrix. There is a good agreement between outcomes of this study and the numerical and experimental results previously reported by Refs. [39,40].

The energy dissipated by the crack growth process, due to different coefficients of thermal expansion for the matrix and reinforcement in composite 2, is depicted in Fig. 14. As expected, the dissipated energy increases during the cooling process.

### 3.2.2. Effect of crack on heat conduction

Assume that the deformed crack surfaces getting away from each other. In such case, due to the crack propagation, the specimen will be divided into smaller pieces, there is negligible heat conduction between separated parts of the material. Hence, the crack can be assumed as an insulator against the heat conduction. To apply such an assumption on the process of the simulation, the coefficient of the heat conduction is reduced by the degradation function  $g(d)$ . Fig. 15a shows the geometric properties and the boundary conditions of a specimen has a crack at the internal corner. The initial temperature of all points of the specimen is 20°C. The heating process is instantaneously induced by a prescribed temperature ( $-900^\circ\text{C}$ ) at the bottom and left side surfaces of the sample. Fig. 15b demonstrates the final distribution of the phase field variable as well as the path of the crack propagation for the thermo-mechanical simulation. Temperature distribution through the specimen is shown in Fig. 16 at three different stages of the simulation to investigate the effect of the heat conduction reduction with crack propagation. It is obvious that the crack acts such as an insulator against the heat conduction and controls the thermal distribution.

The prescribed temperature is changed to investigate its effect in this simulation. The temperature values of 250°C, 500°C and 900°C are used. The obtained load-displacement curves, the crack surface energy and the bulk energy are depicted in Fig. 17. The results are computed at the top of the specimen until the complete splitting of the sample as shown in Fig. 16c. Since the top and bottom surfaces of the sample are constrained in Y-direction, temperature rising produces compressive stress in the sample. In addition, the crack driving force is due to tensile stress. Therefore, the load grew to produce required driving force for crack growth. This effect is well demonstrated in Fig. 17a. As evidenced, when the prescribed temperature is 900°C, the load level increases until the last steps of crack growth and sample splitting. Comparing to results of 250°C and 500°C, minimizing the applied temperature break the sample with small strain due to the reduction of compressive stresses inside the specimen with respect to the higher applied temperature.

### 3.2.3. Thermal shock

This example demonstrates the evolution of thermally induced complex crack patterns in brittle solids. The geometry of an arc sample used

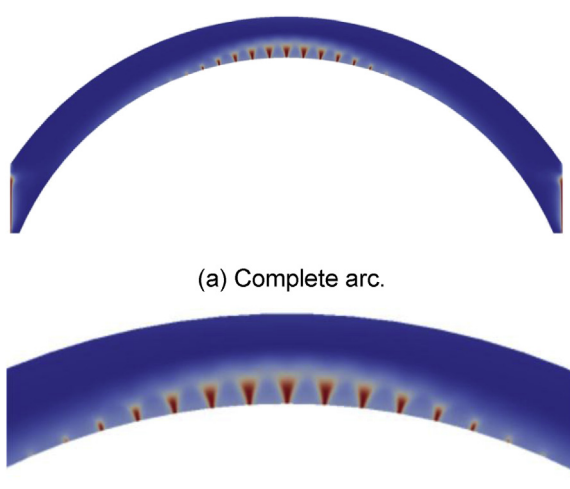


**Fig. 20.** Phase field distribution due to thermal shock.

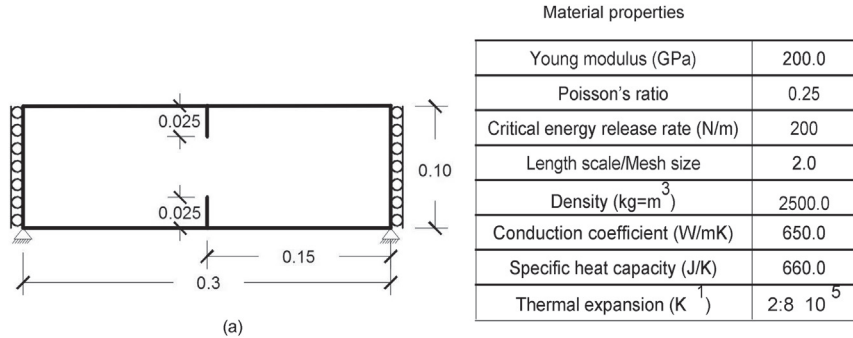


Fig. 21. 3D DENT sample geometry and boundary conditions. The sample thickness is 0.01 m. Dimensions are in m.

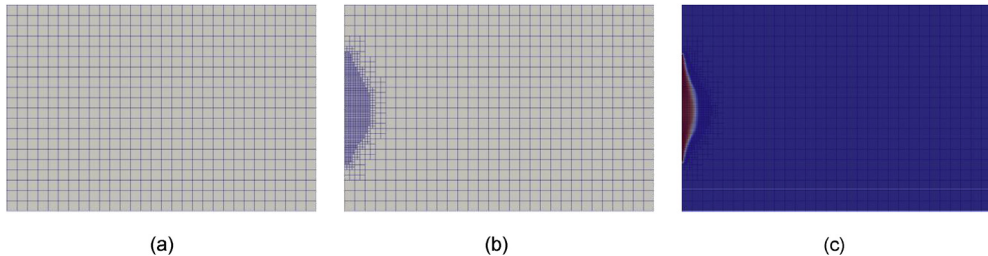


Fig. 22. (a) Initial mesh, (b) Adaptive refined mesh, (c) Crack path. Refinement limit  $R_f = 0.5$  and refinement cycle = 3.

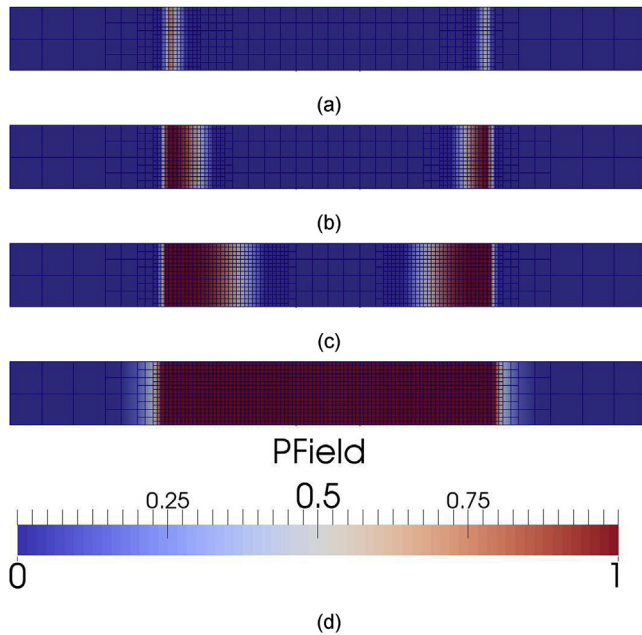


Fig. 23. A cross section at the notches showing the crack steps after 6, 7, 8, and 10 s, respectively.

in this simulation as shown in Fig. 18. The sample is discretized with linear four nodes brick elements. Both ends of the sample are fixed and all other surfaces are free. The thermal shock enforced in the sample by cooling. The cooling process is induced by a prescribed temperature at the inner surface of the arc. The prescribed temperature is reduced from  $20^\circ\text{C}$  to  $-50^\circ\text{C}$  in a time period of 50 s (Fig. 18b). The surface temperature decreases linearly as a ramp function with a time increment of 2 s. The temperature is kept constant at the outer surface. The temperature decrease at the inner surface leads to contraction and a transversely tensile stress in the sample. Once the resulting driving force due to induced

tensile stress exceeds the critical value, cracks initiate. The first crack initiation occurs at the ends of the sample (Fig. 19). When cooling continues, more cracks initiate at the center of the sample and the existing ones grow (Fig. 20). The depth of the damaged zone is increasing and the cracks grow deeper. Finally the cracks form a honeycomb structure at the center of the arc. This simulation shows the ability of the proposed phase field formulation of fracture to predict crack nucleation and complex crack propagation patterns.

### 3.2.4. 3D double notched specimen subjected to thermal load

A 3D double notch specimen is used to examine the crack occur due to thermal convection. The sample geometry, properties, and its boundary conditions are given in Fig. 21. Using the advantage of symmetry, half of the sample is utilized in the simulation. The sample subjected to an initial temperature of  $200^\circ\text{C}$  and decreased to  $190^\circ\text{C}$  in 10 s. Due to temperature decrease, the tensile stresses stimulated at the mid-section of the whole sample where the initial crack notches. The crack started from the notch tip towards the center from both directions, and the mesh gets refined at that zone as shown in Fig. 22. The crack propagation steps are depicted in Fig. 23.

### 3.3. Computational cost

The 2D shear and composite 2 tests with a globally pre-refined mesh, is considered to investigate the computational costs with and without adaptive refinement. The computations are performed using the developed finite element code, on a laptop with an Intel core i5 processor and 2.4 GHz clock rate and 4 GB RAM to compare the computational costs. For the 2D shear test, the computational times are compared for the simulations with global refinement with 16384 elements and 50115 Dofs, the pre-refined mesh in which the mesh is refined in the bottom left of the sample at the first step and kept constant during the rest which leads to a simulation with 5995 elements and 18579 Dofs, and the simulation with adaptive mesh refinement which initially has 1024 elements and 3315 Dofs. For the composite test, the computational times are compared for the simulations with global refinement with 47808 elements and 192516 Dofs and the simulation with adaptive

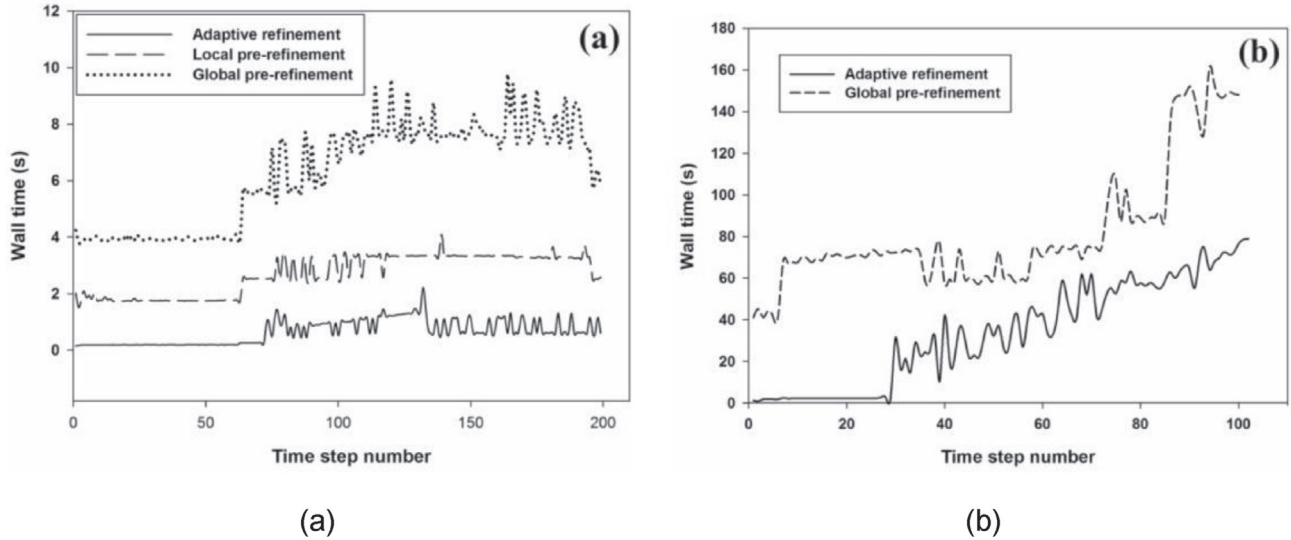


Fig. 24. Comparison of computational cost in terms of the wall clock time for (a) 2D shear test, and (b) Composite 2. The wall clock time is measured for each time step.

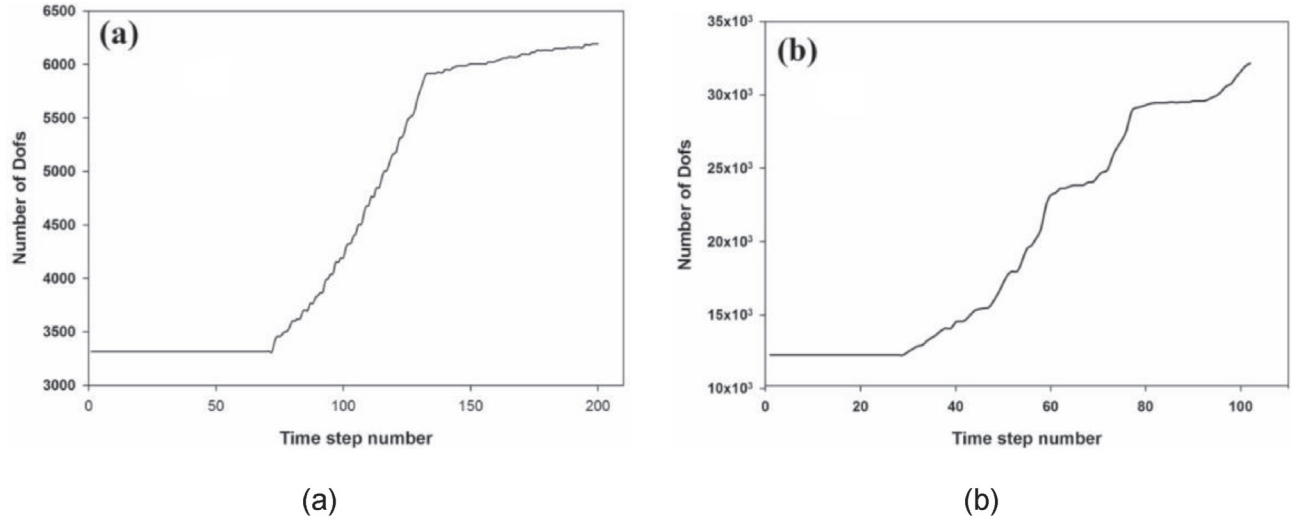


Fig. 25. Evolution of the degrees of freedom during adaptive refinement (a) 2D shear test, (b) Composite 2.

mesh refinement which initially has 2988 elements and 12276 Dofs. Since in most of the simulated examples, the number of Dofs is less than 100 k, the UMFPACK direct solver is used. The wall clock times for these simulations are depicted in Fig. 24. For all simulations, the wall clock time increases when the cracks start to grow (time step 75 for the shear test and 30 for composite 2). Evolution of the degrees of freedom during adaptive refinement is demonstrated in Fig. 25. As demonstrated in Fig. 25, for the simulation with adaptive refinement, the average computational time and the degrees of freedoms are much less the ones for the global pre-refinements. The obtained results prove that the adaptive refinement method saves the computational costs.

#### 4. Conclusion

In this work, a 3D phase field model with a predictor-corrector mesh adaptivity strategy is developed for solving thermo-mechanical

fracture problems. The crack driving force is generalized to thermo-mechanical criteria with the constitutive modeling of the heat conduction through the body. Heat conduction reduction across cracks and heat convection on the external surfaces and their effects on the cracks evolution are investigated. The multi-field problems are solved using a staggered algorithm, and obtained results prove that the approach is computationally efficient and accurate. The performance of the thermo-mechanical phase field formulation of brittle fracture is investigated by means of representative numerical examples. In addition, accuracy, computational cost and time, and the efficiency of the predictor-corrector mesh adaptivity algorithm are investigated on different parameters and benchmark tests. Our findings regarding the computational cost demonstrate that the utilized adaptive refinement method significantly reduces the computational time.

## Appendix A. The consistent tangent operator

The computation of the consistent tangent operator for the model without the crack closure effect as well as without decomposition is easy,

$$\mathbf{D}^{\text{ed}} = [(1-d)^2 + k] \mathbf{C}^e \quad (52)$$

However, for the model with the crack closure effect, with the principal stress derivative at hand, the consistent tangent operator can be computed as the derivative of a general isotropic tensor function [56]. For a two-dimensional case it can be calculated as,

$$\mathbf{D}^{\text{ed}} = \begin{cases} \frac{\sigma_1 - \sigma_2}{\varepsilon_1 - \varepsilon_2} [\mathbf{I}_s - \mathbf{E}_1 \otimes \mathbf{E}_1 - \mathbf{E}_2 \otimes \mathbf{E}_2] + \sum_{i=1}^2 \sum_{j=1}^2 \frac{\partial \sigma_i}{\partial \varepsilon_j} E_i E_j & \text{if } \varepsilon_1 \neq \varepsilon_2 \\ \left[ \frac{\partial \sigma_1}{\partial \varepsilon_1} - \frac{\partial \sigma_1}{\partial \varepsilon_2} \right] \mathbf{I}_s + \frac{\partial \sigma_1}{\partial \varepsilon_2} \mathbf{I} \otimes \mathbf{I} & \text{if } \varepsilon_1 = \varepsilon_2 \end{cases} \quad (53)$$

in which  $\sigma_i$  and  $\varepsilon_i$  are the principal values of the stress and strain tensors, respectively, and  $\mathbf{E}_i$  denotes the eigen-projections of the strain and stress tensors. The principal values of the stress and the corresponding stress tensor can be determined as follow,

$$\sigma_i = [(1-d)^2 + k] (\lambda \langle \varepsilon_1 + \varepsilon_2 + \varepsilon_3 \rangle_+ + 2G \langle \varepsilon_i \rangle_+) + \lambda \langle \varepsilon_1 + \varepsilon_2 + \varepsilon_3 \rangle_- + 2G \langle \varepsilon_i \rangle_- \quad (54)$$

$$\sigma = \sum_{i=0}^3 \sigma_i \mathbf{e}_i \otimes \mathbf{e}_i = [(1-d)^2 + k] (\lambda \langle \varepsilon_1 + \varepsilon_2 + \varepsilon_3 \rangle_+ \mathbf{I} + 2G \varepsilon_+) + (\lambda \langle \varepsilon_1 + \varepsilon_2 + \varepsilon_3 \rangle_- \mathbf{I} + 2G \varepsilon_-) \quad (55)$$

where  $\langle x \rangle_+ := (|x| + x)/2$  and  $\langle x \rangle_- := (x - |x|)/2$ . In a three dimension case the derivation of a general isotropic tensor function is complex especially when the strain tensor has repeated eigenvalues. The final formulations are,

$$\mathbf{D}^{\text{ed}} = \begin{cases} \sum_{a=1}^3 \frac{\sigma_a}{(\varepsilon_a - \varepsilon_b)(\varepsilon_a - \varepsilon_c)} \left\{ \frac{d\varepsilon^2}{dX} - (\varepsilon_b + \varepsilon_c) \mathbf{I}_s - [(\varepsilon_a - \varepsilon_b) + (\varepsilon_a - \varepsilon_c)] \mathbf{E}_a \otimes \mathbf{E}_a \right. \\ \left. - (\varepsilon_b - \varepsilon_c) (\mathbf{E}_b \otimes \mathbf{E}_b - \mathbf{E}_c \otimes \mathbf{E}_c) \right\} + \sum_{i=1}^3 \sum_{j=1}^3 \frac{\partial \sigma_i}{\partial \varepsilon_j} \mathbf{E}_i \otimes \mathbf{E}_j & \text{if } \varepsilon_1 \neq \varepsilon_2 \neq \varepsilon_3 \\ b_1 \frac{d\varepsilon^2}{dX} - b_2 \mathbf{I}_s - b_3 \varepsilon \otimes \varepsilon + b_4 \varepsilon \otimes \mathbf{I} + b_5 \mathbf{I} \otimes \varepsilon - b_6 \mathbf{I} \otimes \mathbf{I} & \text{if } \varepsilon_a \neq \varepsilon_b = \varepsilon_c \\ \left[ \frac{\partial \sigma_1}{\partial \varepsilon_1} - \frac{\partial \sigma_1}{\partial \varepsilon_2} \right] \mathbf{I}_s + \frac{\partial \sigma_1}{\partial \varepsilon_2} \mathbf{I} \otimes \mathbf{I} & \text{if } \varepsilon_1 = \varepsilon_2 = \varepsilon_3 \end{cases} \quad (56)$$

where  $\frac{d\varepsilon^2}{dX}$  indicates the derivative of the square of the strain tensor with Cartesian components and can be determined as,

$$\left[ \frac{d\varepsilon^2}{dX} \right]_{ijkl} = \frac{1}{2} (\delta_{ik}\varepsilon_{lj} + \delta_{il}\varepsilon_{kj} + \delta_{jl}\varepsilon_{ik} + \delta_{kj}\varepsilon_{il}) \quad (57)$$

and (a, b, c) are cyclic permutations of (1, 2, 3). The scalar values b1-b6 are defined as,

$$b_1 = \frac{\sigma_a - \sigma_c}{(\varepsilon_a - \varepsilon_c)^2} + \frac{1}{(\varepsilon_a - \varepsilon_c)} \left( \frac{\partial \sigma_c}{\partial \varepsilon_b} - \frac{\partial \sigma_c}{\partial \varepsilon_c} \right) \quad (58)$$

$$b_2 = 2\varepsilon_c \frac{\sigma_a - \sigma_c}{(\varepsilon_a - \varepsilon_c)^2} + \frac{\varepsilon_a + \varepsilon_c}{(\varepsilon_a - \varepsilon_c)} \left( \frac{\partial \sigma_c}{\partial \varepsilon_b} - \frac{\partial \sigma_c}{\partial \varepsilon_c} \right) \quad (59)$$

$$b_3 = 2 \frac{\sigma_a - \sigma_c}{(\varepsilon_a - \varepsilon_c)^3} + \frac{1}{(\varepsilon_a - \varepsilon_c)^2} \left( \frac{\partial \sigma_a}{\partial \varepsilon_c} + \frac{\partial \sigma_c}{\partial \varepsilon_a} - \frac{\partial \sigma_a}{\partial \varepsilon_a} - \frac{\partial \sigma_c}{\partial \varepsilon_c} \right) \quad (60)$$

$$b_4 = 2\varepsilon_c \frac{\sigma_a - \sigma_c}{(\varepsilon_a - \varepsilon_c)^3} + \frac{1}{(\varepsilon_a - \varepsilon_c)} \left( \frac{\partial \sigma_a}{\partial \varepsilon_c} - \frac{\partial \sigma_c}{\partial \varepsilon_b} \right) + \frac{\varepsilon_c}{(\varepsilon_a - \varepsilon_c)^2} \left( \frac{\partial \sigma_a}{\partial \varepsilon_c} + \frac{\partial \sigma_c}{\partial \varepsilon_a} - \frac{\partial \sigma_a}{\partial \varepsilon_a} - \frac{\partial \sigma_c}{\partial \varepsilon_c} \right) \quad (61)$$

$$b_5 = 2\varepsilon_c \frac{\sigma_a - \sigma_c}{(\varepsilon_a - \varepsilon_c)^3} + \frac{1}{(\varepsilon_a - \varepsilon_c)} \left( \frac{\partial \sigma_c}{\partial \varepsilon_a} - \frac{\partial \sigma_c}{\partial \varepsilon_b} \right) + \frac{\varepsilon_c}{(\varepsilon_a - \varepsilon_c)^2} \left( \frac{\partial \sigma_a}{\partial \varepsilon_c} + \frac{\partial \sigma_c}{\partial \varepsilon_a} - \frac{\partial \sigma_a}{\partial \varepsilon_a} - \frac{\partial \sigma_c}{\partial \varepsilon_c} \right) \quad (62)$$

$$b_6 = 2\varepsilon_c^2 \frac{\sigma_a - \sigma_c}{(\varepsilon_a - \varepsilon_c)^3} + \frac{\varepsilon_a \varepsilon_c}{(\varepsilon_a - \varepsilon_c)^2} \left( \frac{\partial \sigma_a}{\partial \varepsilon_c} + \frac{\partial \sigma_c}{\partial \varepsilon_a} \right) - \frac{\varepsilon_c^2}{(\varepsilon_a - \varepsilon_c)^2} \left( \frac{\partial \sigma_a}{\partial \varepsilon_a} + \frac{\partial \sigma_c}{\partial \varepsilon_c} \right) - \frac{\varepsilon_a + \varepsilon_c}{\varepsilon_a - \varepsilon_c} \frac{\partial \sigma_c}{\partial \varepsilon_b} \quad (63)$$

## References

- [1] S. Shimamura, Y. Sotoike, Computer modeling of thermal shock-induced crack growth in brittle materials, *J. Mater. Res.* 7 (05) (1992) 1286–1291.
- [2] P. Areias, M.A. Msekh, T. Rabczuk, Damage and fracture algorithm using the screened poisson equation and local remeshing, *Eng. Fract. Mech.* 158 (2016) 116–143.
- [3] T. Rabczuk, T. Belytschko, Cracking particles: a simplified meshfree method for arbitrary evolving cracks, *Int. J. Numer. Methods Eng.* 61 (13) (2004) 2316–2343.
- [4] T. Rabczuk, J.H. Song, T. Belytschko, Simulations of instability in dynamic fracture by the cracking particles method, *Eng. Fract. Mech.* 76 (6) (2009) 730–741.
- [5] T. Rabczuk, T. Belytschko, A three-dimensional large deformation meshfree method for arbitrary evolving cracks, *Comput. Methods Appl. Mech. Eng.* 196 (29) (2007) 2777–2799.
- [6] H. Ren, X. Zhuang, Y. Cai, T. Rabczuk, Dual-horizon peridynamics, *Int. J. Numer. Methods Eng.* 108 (12) (2016) 1451–1476.
- [7] H. Ren, X. Zhuang, T. Rabczuk, Dual-horizon peridynamics: a stable solution to varying horizons, *Comput. Methods Appl. Mech. Eng.* 318 (2017) 762–782.
- [8] A. Griffith, The phenomena of rupture and flow in solids, *Philos. Trans. R. Soc. Lond. A* 221 (1921) 163–198.
- [9] G.A. Francfort, J.J. Marigo, Revisiting brittle fracture as an energy minimization problem, *J. Mech. Phys. Solids* 46 (8) (1998) 1319–1342.

- [10] H. Amor, J.J. Marigo, C. Maurini, Regularized formulation of the variational brittle fracture with unilateral contact: numerical experiments, *J. Mech. Phys. Solids* 57 (8) (2009) 1209–1229.
- [11] M.J. Borden, C.V. Verhoosel, M.A. Scott, T.J. Hughes, C.M. Landis, A phase-field description of dynamic brittle fracture, *Comput. Methods Appl. Mech. Eng.* 217 (2012) 77–95.
- [12] B. Bourdin, G.A. Francfort, J.J. Marigo, The variational approach to fracture, *J. Elast.* 91 (1–3) (2008) 5–148.
- [13] B. Bourdin, Numerical implementation of the variational formulation for quasi-static brittle fracture, *Interfaces Free Boundaries* 9 (3) (2007) 411–430.
- [14] B. Bourdin, G.A. Francfort, J.J. Marigo, Numerical experiments in revisited brittle fracture, *J. Mech. Phys. Solids* 48 (4) (2000) 797–826.
- [15] C. Miehe, F. Welschinger, M. Hofacker, Thermodynamically consistent phase-field models of fracture: variational principles and multi-field fe implementations, *Int. J. Numer. Methods Eng.* 83 (10) (2010) 1273–1311.
- [16] M.J. Borden, T.J. Hughes, C.M. Landis, C.V. Verhoosel, A higher-order phase-field model for brittle fracture: formulation and analysis within the isogeometric analysis framework, *Comput. Methods Appl. Mech. Eng.* 273 (2014) 100–118.
- [17] M.A. Msekh, J.M. Sargado, M. Jamshidian, P.M. Areias, T. Rabczuk, Abaqus implementation of phase-field model for brittle fracture, *Comput. Mater. Sci.* 96 (2015) 472–484.
- [18] M. Ambati, T. Gerasimov, L. De Lorenzis, A review on phase-field models of brittle fracture and a new fast hybrid formulation, *Comput. Mech.* 55 (2) (2015) 383–405.
- [19] P. Areias, T. Rabczuk, M. Msekh, Phase-field analysis of finite-strain plates and shells including element subdivision, *Comput. Methods Appl. Mech. Eng.* 312 (2016) 322–350.
- [20] F. Amiri, D. Millán, Y. Shen, T. Rabczuk, M. Arroyo, Phase-field modeling of fracture in linear thin shells, *Theor. Appl. Fract. Mech.* 69 (2014) 102–109.
- [21] J. Reinoso, M. Paggi, C. Linder, Phase field modeling of brittle fracture for enhanced assumed strain shells at large deformations: formulation and finite element implementation, *Comput. Mech.* 59 (6) (2017) 981–1001.
- [22] A. Schlüter, A. Willenbücher, C. Kuhn, R. Müller, Phase field approximation of dynamic brittle fracture, *Comput. Mech.* 54 (5) (2014) 1141–1161.
- [23] G. Liu, Q. Li, M.A. Msekh, Z. Zuo, Abaqus implementation of monolithic and staggered schemes for quasi-static and dynamic fracture phase-field model, *Comput. Mater. Sci.* 121 (2016) 35–47.
- [24] C. Miehe, F. Aldakheel, S. Teichtmeister, Phase-field modeling of ductile fracture at finite strains: a robust variational-based numerical implementation of a gradient-extended theory by micromorphic regularization, *Int. J. Numer. Methods Eng.* 111 (9) (2017) 816–863.
- [25] M. Ambati, R. Kruse, L. De Lorenzis, A phase-field model for ductile fracture at finite strains and its experimental verification, *Comput. Mech.* 57 (1) (2016) 149–167.
- [26] H. Badnava, E. Etemadi, M.A. Msekh, A phase field model for rate-dependent ductile fracture, *Metals* 7 (5) (2017) 180.
- [27] C. Miehe, S. Mauthe, S. Teichtmeister, Minimization principles for the coupled problem of darcy-biot-type fluid transport in porous media linked to phase field modeling of fracture, *J. Mech. Phys. Solids* 82 (2015) 186–217.
- [28] C. Miehe, S. Mauthe, Phase field modeling of fracture in multi-physics problems. part III. crack driving forces in hydro-poro-elasticity and hydraulic fracturing of fluid-saturated porous media, *Comput. Methods Appl. Mech. Eng.* 304 (2016) 619–655.
- [29] A. Mikelic, M.F. Wheeler, T. Wick, A phase-field method for propagating fluid-filled fractures coupled to a surrounding porous medium, *Multiscale Model. Simul.* 13 (1) (2015) 367–398.
- [30] A. Mikelić, M.F. Wheeler, T. Wick, A quasi-static phase-field approach to pressurized fractures, *Nonlinearity* 28 (5) (2015) 1371.
- [31] M. Wheeler, T. Wick, W. Wollner, An augmented-lagrangian method for the phase-field approach for pressurized fractures, *Comput. Methods Appl. Mech. Eng.* 271 (2014) 69–85.
- [32] B. Bourdin, J.J. Marigo, C. Maurini, P. Sicsic, Morphogenesis and propagation of complex cracks induced by thermal shocks, *Phys. Rev. Lett.* 112 (1) (2014):014301.
- [33] T. Wick, Coupling fluid–structure interaction with phase-field fracture, *J. Comput. Phys.* 327 (2016) 67–96.
- [34] C. Miehe, M. Hofacker, L.M. Schaenzel, F. Aldakheel, Phase field modeling of fracture in multi-physics problems. part II. coupled brittle-to-ductile failure criteria and crack propagation in thermo-elastic-plastic solids, *Comput. Methods Appl. Mech. Eng.* 294 (2015) 486–522.
- [35] C. Miehe, L.M. Schaenzel, H. Ulmer, Phase field modeling of fracture in multi-physics problems. part I. balance of crack surface and failure criteria for brittle crack propagation in thermo-elastic solids, *Comput. Methods Appl. Mech. Eng.* 294 (2015) 449–485.
- [36] M.A. Msekh, M. Silani, M. Jamshidian, P. Areias, X. Zhuang, G. Zi, P. He, T. Rabczuk, Predictions of j integral and tensile strength of clay/epoxy nanocomposites material using phase field model, *Compos. Part B Eng.* 93 (2016) 97–114.
- [37] M.A. Msekh, N. Cuong, G. Zi, P. Areias, X. Zhuang, T. Rabczuk, Fracture properties prediction of clay/epoxy nanocomposites with interphase zones using a phase field model, *Eng. Fract. Mech.* (2017) <https://doi.org/10.1016/j.engfracmech.2017.08.002> (in press).
- [38] Y. Fu, Y. Wong, C. Tang, C. Poon, Thermal induced stress and associated cracking in cement-based composite at elevated temperatures—part i: thermal cracking around single inclusion, *Cem. Concr. Compos.* 26 (2) (2004) 99–111.
- [39] D.L. Hiemstra, N. Sottos, Thermally induced interfacial microcracking in polymer matrix composites, *J. Compos. Mater.* 27 (10) (1993) 1030–1051.
- [40] R. Davidge, T.J. Green, The strength of two-phase ceramic/glass materials, *J. Mater. Sci.* 3 (6) (1968) 629–634.
- [41] H. Badnava, M. Kadkhodaei, M. Mashayekhi, Modeling of unstable behaviors of shape memory alloys during localization and propagation of phase transformation using a gradient-enhanced model, *J. Intell. Mater. Syst. Struct.* 26 (18) (2015) 2531–2546.
- [42] H. Badnava, M. Kadkhodaei, M. Mashayekhi, A non-local implicit gradient-enhanced model for unstable behaviors of pseudoelastic shape memory alloys in tensile loading, *Int. J. Solids Struct.* 51 (23) (2014) 4015–4025.
- [43] R. de Borst, C.V. Verhoosel, Gradient damage vs phase-field approaches for fracture: similarities and differences, *Comput. Methods Appl. Mech. Eng.* 312 (2016) 78–94.
- [44] T. Heister, M.F. Wheeler, T. Wick, A primal-dual active set method and predictor-corrector mesh adaptivity for computing fracture propagation using a phase-field approach, *Comput. Methods Appl. Mech. Eng.* 290 (2015) 466–495.
- [45] B. Bourdin, G. Francfort, J.J. Marigo, Numerical experiments in revisited brittle fracture, *J. Mech. Phys. Solids* 48 (2000) 797–826.
- [46] S. Burke, C. Ortner, E. Süli, An adaptive finite element approximation of a variational model of brittle fracture, *SIAM J. Numer. Anal.* 48 (3) (2010) 980–1012.
- [47] A. Mesgarnejad, B. Bourdin, M. Khonsari, Validation simulations for the variational approach to fracture, *Comput. Methods Appl. Mech. Eng.* 290 (2015) 420–437.
- [48] C. Miehe, M. Hofacker, F. Welschinger, A phase field model for rate-independent crack propagation: robust algorithmic implementation based on operator splits, *Comput. Methods Appl. Mech. Eng.* 199 (2010) 2765–2778.
- [49] P. Areias, E. Samaniego, T. Rabczuk, A staggered approach for the coupling of cahn-hilliard type diffusion and finite strain elasticity, *Comput. Mech.* 57 (2) (2016) 339–351.
- [50] P. Areias, T. Rabczuk, J. César de Sá, A novel two-stage discrete crack method based on the screened poisson equation and local mesh refinement, *Comput. Mech.* 58 (6) (2016) 1003–1018.
- [51] P. Areias, J. Reinoso, P. Camanho, T. Rabczuk, A constitutive-based element-by-element crack propagation algorithm with local mesh refinement, *Comput. Mech.* 56 (2) (2015) 291–315.
- [52] W. Bangerth, D. Davydov, T. Heister, L. Heltai, G. Kanschat, M. Kronbichler, M. Maier, B. Turcksin, D. Wells, The deal. ii library, version 8.4, *J. Numer. Math.* 24 (2016) 135–141.
- [53] W. Bangerth, T. Heister, G. Kanschat, et al., Deal. II Differential Equations Analysis Library, 2013. <http://www.dealii.org>.
- [54] C. Shi, A.G. van Dam, J.G. van Mier, B. Sluys, Crack interaction in concrete, *Mater. Build. Struct.* 6 (2005) 125–131.
- [55] H. Badnava, M. Mashayekhi, M. Kadkhodaei, An anisotropic gradient damage model based on microplane theory, *Int. J. Damage Mech.* 25 (3) (2015) 336–357.
- [56] E.A. de Souza Neto, D. Peric, D.R. Owen, Computational Methods for Plasticity: Theory and Applications, John Wiley & Sons, 2011.